

THE FLORIDA STATE UNIVERSITY
COLLEGE OF ARTS AND SCIENCES

ASSIMILATION OF FSU AND NCEP REANALYSIS PSEUDOSTRESS
PRODUCTS OVER THE PACIFIC OCEAN AND COMPLEX EOF ANALYSIS
OF THE RESULTING FIELDS.

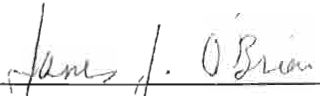
By

WILLIAM M. PUTMAN

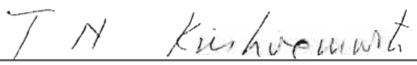
A Thesis submitted to the
Department of Meteorology
in partial fulfillment of the
requirements for the degree of
Master of Science

Degree Awarded:
Summer Semester, 1998

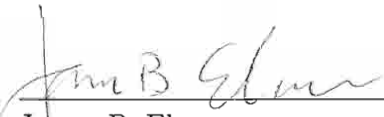
The members of the Committee approve the thesis of William M.
Putman defended on June 18, 1998.



James J. O'Brien
Professor Directing Thesis



T. N. Krishnamurti
Committee Member



James B. Elsner
Committee Member

Approved:



Peter Ray, Chair, Department of Meteorology

Peter Ray, Chair, Department of Meteorology

ACKNOWLEDGEMENTS

I would like to thank my major professor, Dr. James O'Brien, for his guidance, and enlightening discussions throughout the course of my studies here at Florida State University. I am grateful to my thesis committee members, Dr. T. N. Krishnamurti, and Dr. James B. Elsner for their constructive comments and support of this research. My sincere gratitude is extended to Dr. David M. Legler for his continued support and tutelage throughout the course of this research. A special thanks is extended to the staff and members of the Center for Ocean Atmospheric Prediction Studies for their support and comments, in particular Jiraporn Whalley for her assistance in continuing to develop my graphics skills, and Dr. Mark Bourassa for his support in dealing with the minimization code applied in this research. In addition, I would like to thank each of my fellow graduate students for the friendship and riveting conversations, as well as my family and fiancée for their limitless support and encouragement.

This research was supported by the National Science Foundation, Office of Naval Research, and the National Oceanic and Atmospheric Administration, under grants NAGW-985, and grants supporting the WOCE Center for Surface Meteorology and Fluxes (OCE-9314515). NCEP Reanalysis data was provided by NOAA Climate Diagnostics Center, Boulder, Colorado; UWM/COADS climatology provided courtesy of Dr. Arlindo da Silva.

TABLE OF CONTENTS

LIST OF FIGURES	vi
ABSTRACT	ix
1. INTRODUCTION	1
2. DATA	4
2.1 FSU Tropical Pacific Pseudostress	4
2.2 NCEP Reanalysis	6
2.3 UWM/COADS Climatology	9
3. METHODOLOGY	10
3.1 The Cost Function	11
3.2 Minimization with the Conjugate-Gradient Method	13
3.3 CEOF Analysis	14
4. RESULTS	16
4.1 FSU and NCEP Weight Selection	16
4.2 Sensitivity Results	17
4.3 Final Direct Minimization Results	25
4.4 CEOF results	34
The First Principal Component	41
The Second Principal Component	42
The Third Principal Component	43
The Fourth Principal Component	44
The Third Principal Component	43
The Fourth Principal Component	44
The 1982-83 El Niño Event	45

The 1972-73 El Niño Event	46
The El Niño Events of the 1960's	47
The 1988-89 El Viejo Event	48
5. SUMMARY	68
REFERENCES	71
BIOGRAPHICAL SKETCH	73

LIST OF FIGURES

1	Average magnitude of the NCEP reanalysis pseudostress minus the average magnitude of the FSU pseudostress, with difference vectors. The averages are over all October values from 1961-1997.	7
2	Average divergence of the NCEP reanalysis pseudostress minus the average divergence of the FSU pseudostress. The averages are over all October values from 1961-1997.	8
3	FSU and NCEP weights	12
4	August 1991 pseudostress magnitude response function as a function of the Laplacian weight.	19
5	Same as figure 4 except the divergence weight varies.	20
6	Same as figure 4 except the curl weight varies.	22
7	August 1991 pseudostress divergence response function as a function of the Laplacian weight.	23
8	The climatology weighting region.	24
9	FSU pseudostress magnitude and vectors, August 1991.	26
10	Magnitude of direct minimization solution with kinematic weights set to zero minus the magnitude of the solution with nonzero kinematic weights.	27
11	FSU pseudostress divergence, August 1991.	28
12	Divergence of direct minimization solution with kinematic weights set to zero minus the divergence of the solution with nonzero kinematic weights.	29
13	Magnitude of the minimization solution pseudostress with vectors, for August 1991.	31
14	Magnitude of the minimization solution pseudostress minus the magnitude of the NCEP pseudostress with difference vectors, for August 1991.	32
15	Same as figure 14, except the difference is with respect to FSU pseudostress magnitude.	33
15	Same as figure 14, except the difference is with respect to FSU pseudostress magnitude.	33

16	Magnitude of the minimization solution pseudostress minus the magnitude of the NCEP reanalysis pseudostress along the 135° W longitude band versus time.	35
17	Same as figure 16, except the difference is with respect to FSU pseudostress magnitude.	36
18	Average divergence of the minimization solution pseudostress minus the average divergence of the NCEP reanalysis pseudostress.	37
19	Divergence of minimization solution pseudostress minus the divergence of the NCEP pseudostress along the 135° W longitude band versus time.	38
20	Same as figure 18 except the difference is with respect to FSU pseudostress divergence.	39
21	The first spatial function from the CEOF analysis. This field represents 22.76 percent of the variance.	50
22	The amplitude(top) and rotation angle(bottom) for the first eigenvector, and JMA SST index(blue).	51
23	The second spatial function from the CEOF analysis. This field represents 11.16 percent of the variance.	52
24	The amplitude(top) and rotation angle(bottom) for the second eigenvector, and JMA SST index(blue).	53
25	The third spatial function from the CEOF analysis. This field represents 10.01 percent of the variance.	54
26	The amplitude(top) and rotation angle(bottom) for the third eigenvector, and JMA SST index(blue).	55
27	The fourth spatial function from the CEOF analysis. This field represents 7.02 percent of the variance.	56
28	The amplitude(top) and rotation angle(bottom) for the fourth eigenvector, and JMA SST index(blue).	57
29	The amplitude for the first through fourth eigenvectors from January of 1982 through December of 1983, and JMA SST anomaly index(blue).	58
30	The rotation angle for the first through fourth eigenvectors from January of 1982 through December of 1983.	59
31	Same as figure 29 except from January of 1972 through December of 1973.	60
32	Same as figure 30 except from January of 1972 through December of 1973.	61

33	Same as figure 29 except from January of 1964 through December of 1966.	62
34	Same as figure 30 except from January of 1964 through December of 1966.	63
35	Same as figure 29 except from January of 1962 through December of 1963.	64
36	Same as figure 30 except from January of 1962 through December of 1963.	65
37	Same as figure 29 except from January of 1988 through December of 1989.	66
38	Same as figure 30 except from January of 1988 through December of 1989.	67

ABSTRACT

A variational technique is applied in the blending of height-adjusted Florida State University (FSU) and National Centers for Environmental Prediction (NCEP) reanalysis monthly 10-meter pseudostress vectors over the Pacific Ocean. The analyses cover the time period from 1961 through 1997, over the domain of 40° S to 40° N, and 125° E to 70° W. A cost function is designed consisting of five constraints; each constraint is given a weighting coefficient which determines its influence on the minimization solution. The first two constraints are misfits for the FSU and NCEP reanalysis datasets. Climatological structure information is used as a weak constraint on the solution through Laplacian and kinematic (divergence, and curl) constraints on the cost function. A spatially dependent weighting is designed for the misfit constraints, which highlights the regional strengths of each dataset. The weights for the climatological constraints are selected using a sensitivity analysis which studies the impact of each constraint on the solution by varying its coefficient. The cost function is minimized using the conjugate-gradient method.

Case studies are highlighted, and reveal the impact each term of the cost function has on the minimization solution. Analyses of all months reveal the successful distribution of the regional strengths of each dataset by the spatially dependent weighting. NCEP reanalysis data, from 40° N to 60° N, are added to the minimization solution fields, and the monthly mean climatologies, calculated from the solution fields, are removed from the combined fields. The resulting pseudostress anomalies are filtered with an 18-month low-pass filter, and a complex empirical orthogonal function (CEOF) analysis is performed on the filtered anomalies. The CEOF analysis reveals the presence of a strengthening of the Aleutian low in the north Pacific, coincident with (CEOF) analysis is performed on the filtered anomalies. The CEOF analysis reveals the presence of a strengthening of the Aleutian low in the north Pacific, coincident with the anomalous westerlies along the equator associated with El Niño events during the

analysis period. The analysis also reveals a weakening of the Aleutian low during the winter-spring preceding the El Niño events of 1973 and 1983, and during the peak period of El Viejo, the cold phase of the El Niño-Southern Oscillation (ENSO).

1. INTRODUCTION

Accurate surface wind stress and pseudostress fields over the Pacific Ocean are vital in ocean modeling and studies of seasonal and interannual variability of the ocean-atmosphere system. The accuracy of pseudostress products over the tropical Pacific has been the subject of many studies. Modeling experiments, forced with the Florida State University (FSU) pseudostress product, have produced high coherence with observed dynamic height in the western and central tropical Pacific (*McPhaden et al.* (1988)). The FSU product also performs well in studies of model forced ocean circulations as compared to observations (*Landsteiner et al.* (1990)). The National Centers for Environmental Prediction (NCEP) has produced a global reanalysis of atmospheric fields, including surface winds, from 1957 to the present. The NCEP reanalysis provides surface wind data over the entire Pacific Ocean which can be combined with the superior FSU tropical Pacific data into a blended pseudostress field covering the entire Pacific Ocean. This study produces a blended product of FSU and NCEP reanalysis pseudostress over the Pacific Ocean, and examines the relationship between tropical and extratropical regions in the solution on interannual time periods.

A simple blending method would be to piece the two products together, and smooth along the border with a simple spatial interpolation scheme. This does not account for the variations in the reference height of the two products (20 meters for FSU and 10 meters for NCEP). Significant wind shear can exist between 10 and 20 meters above the ocean (*da Silva et al.* (1994)); this shear must be accounted for in FSU and 10 meters for NCEP). Significant wind shear can exist between 10 and 20 meters above the ocean (*da Silva et al.* (1994)); this shear must be accounted for in the blending method. A basic blending method would also lead to inaccuracies in

the derivative fields of the solution, due to discrepancies between the two products along the blending border. A variational approach provides a more robust method of blending the desired fields, while maintaining realistic physical properties in the kinematic fields of the solution.

Variational blending has become a widely used tool in objective analysis. This technique, involving the minimization of a non-linear combination of observations, background information, and other dynamical or physical constraints (Laplacian, curl, divergence, etc.), has been applied when gridding irregularly spaced observations into smoothed analyses (*Hoffman (1984)*). A direct minimization data assimilation approach has been applied to produce monthly pseudostress vector fields, based on insitu surface marine observations and climatological information, over the Indian Ocean (*Legler et al. (1989)*). Variational analysis studies of this type have been able to produce fields which were representative of subjectively analyzed fields. This study applies a similar variational approach in the blending of 10-meter pseudostress analyses from the reference height adjusted FSU wind product, and the NCEP reanalysis, over the Pacific Ocean from 1961 through 1997.

Through the minimization of a strategically designed cost function, it is possible to combine the positive aspects of various datasets, while maintaining realistic physical characteristics in the derivative fields such as divergence and curl. This is accomplished with spatially dependent weighting functions, determined a priori, based on the regional characteristics of each 'observation' dataset, in this case the FSU and NCEP reanalysis datasets. Determining the appropriate weights for the kinematic terms of the cost function is much more challenging. One option is to use the inverse of the estimated error variances of the background field as a weighting function (*Fischer et al. (1997)* and *Lorenc (1986)*). This method relies on the accuracy of the estimated error variances. Sensitivity analysis, an analysis technique which measures the 'sensitivity' of the parameters involved in the direct minimization, is an alternative to the use of estimated error variances. Sensitivity analysis, an analysis technique which measures the 'sensitivity' of the parameters involved in the direct minimization, is an alter-

nate option (*Meyers et al.* (1994)). The sensitivity of a parameter is defined as the change in the solution per change in the parameter. We have applied this technique in determining the optimal weighting for the kinematic terms of our cost function.

The FSU and NCEP reanalysis pseudostress fields are blended using a direct minimization approach to produce a more robust analysis over the Pacific Ocean than is presently available. The reference height of the FSU product is adjusted using a boundary layer model incorporating fields of atmospheric moisture and temperature from the NCEP reanalysis. A spatially dependent weighting scheme is developed based on the regional strengths of each dataset. The weights of the Laplacian and kinematic terms of the cost function are determined by the results of a sensitivity analysis. The direct minimization approach produces the desired blending of the FSU and NCEP reanalysis products, without producing artificial noise in the derivative fields of the solution.

This product has direct applications to improving research of El Niño and the Southern Oscillation (ENSO). Our ability to examine interactions between accurate tropical and extratropical pseudostress over the Pacific Ocean is greatly improved by the existence of this blended product. This study applies complex empirical orthogonal function (CEOF) analysis to the blended solution fields. The CEOF analysis reveals the interannual variability of the analyses, from which physical interpretations of the variability between tropical and extratropical pseudostress are derived; particularly the relationship between the strength of the Aleutian low and ENSO.

2. DATA

The FSU, NCEP reanalysis, and UWM/COADS climatology pseudostress fields are the datasets used in the assimilation. The assimilation, a variational blending process, is intended to accentuate the strengths of each dataset in a more reliable pseudostress field which can provide better forcing in ocean and atmosphere models. For this reason, emphasis will be placed on the regional strengths and weaknesses of each dataset.

2.1 FSU Tropical Pacific Pseudostress

The FSU dataset (e.g., *Stricherz et al.* (1997)) is a subjectively analyzed compilation of monthly ship observations over the tropical Pacific, 30° N to 30° S, 120° E to 70° W, from 1961 to present. An average of 25,000 wind observations each month are converted to pseudostress and binned into 10° longitude by 2° latitude rectangles. Pseudostress is computed from wind data according to

$$\tau_x = u(u^2 + v^2)^{0.5} \quad (1)$$

$$\tau_y = v(u^2 + v^2)^{0.5} \quad (2)$$

where τ_x and τ_y are respectively the eastward and northward components of pseudostress and u and v are respectively the eastward and northward wind components. Statistical methods are used to eliminate “bad” observations for rectangles with more than two observations. The resulting binned data are subjectively analyzed, checked, and digitized onto a 2° by 2° latitude-longitude grid resulting in monthly mean pseudostress fields based on in-situ data from ships, buoys, and other marine station and digitized onto a 2° by 2° latitude-longitude grid resulting in monthly mean pseudostress fields based on in-situ data from ships, buoys, and other marine station observations.

Data coverage, defined as the number of observations for a given analyses rectangle, was good for the Northern Hemisphere. However, areas of the Southern Hemisphere equatorial regions suffer from poor data coverage. The region off the coast of South America from about 12°S to 30°S and extending out to around 120°W is a particularly data sparse area. The FSU analyses are weighted subjectively according to the number of observations and incorporate climatology information in an attempt to deal with these data void regions. Other studies have examined the success of the FSU product in forcing ocean models to resemble observations of sea level and dynamic height (*McPhaden et al. (1988)*) as well as comparisons to other surface wind products (*Landsteiner et al. (1990)*). Results of these studies agree that the lack of observations in the FSU analysis hurt the overall quality of the product in the data sparse regions, particularly in the southeast Pacific off the coast of South America. Therefore, the analyses in this region are particularly suspect and an area which the blending procedure is designed to reduce the FSU influence on the output.

The in-situ observations, on which the FSU analyses are based, are presumably recorded at a height of 20 meters and must be adjusted to the NCEP reanalysis height of 10 meters. Prior studies have shown that under stable conditions at low wind speeds significant wind shear can exist between 10 and 20 meters above the ocean surface (*da Silva et al. (1994)*). Wind stress measured at 10 meters could be as much as 20 to 40 percent of a measurement taken at a height of 20 meters. These variations must be accounted for by analyzing the fields at a constant reference height of 10 meters. Prior to the height adjustment the FSU analyses are bilinearly interpolated to the NCEP Gaussian grid. Fields of atmospheric moisture and temperature from the NCEP reanalysis are used in a boundary layer model to determine height adjustment coefficients for each grid point. These coefficients are then applied to the FSU analyses to create the 10 meter FSU pseudostress fields.

Additional details of the FSU analyses can be found in *Stricherz et al. (1997)*, and to create the 10 meter FSU pseudostress fields.

Additional details of the FSU analyses can be found in *Stricherz et al. (1997)*, and

further diagnostic analysis can be found in *Zebiak* (1990).

2.2 NCEP Reanalysis

The NCEP reanalysis project began in 1991 as the U.S. National Meteorological Center(NMC) Climate Data Assimilation System project. The project's goal is a 40 year global assimilation of land surface, ship, buoy, and other data in fields of atmospheric data. The analysis consists of a spectral statistical interpolation and a three-dimensional variational scheme. Specifics of the NCEP reanalysis scheme can be found in *Kalnay et al.* (1996).

The 10 meter u and v wind components from the surface Gaussian NCEP reanalysis dataset are available every six hours. The six hourly wind components are converted to pseudostress and averaged to create monthly mean NCEP reanalysis pseudostress fields from 1961 to 1997. NCEP classifies the u and v wind components as class A variables. Class A variables are those which are greatly influenced by observational data as opposed to model derived quantities. This is considered the most reliable class of data in the reanalysis. The pseudostress from NCEP reanalysis data are extracted on a Gaussian grid from 40°S to 40°N and 125°E to 70°W.

The NCEP reanalysis pseudostress fields provide a different representation of the southerlies off the coast of South America in the region of poor FSU data coverage (Fig. 1). Analysis of the divergence fields for the NCEP reanalysis and FSU analyses illuminates the problems with the NCEP reanalysis (Fig. 2). The FSU fields produce a well defined intertropical convergence zone(ITCZ) which is practically nonexistent in the NCEP reanalysis. The tropical Pacific is a suspect region for the NCEP reanalysis. Subjective selection of the spatially dependent weight scheme allows us to reduce the impact of the NCEP reanalysis on the solution for these suspect regions, while maintaining its influence at higher latitudes.

while maintaining its influence at higher latitudes.

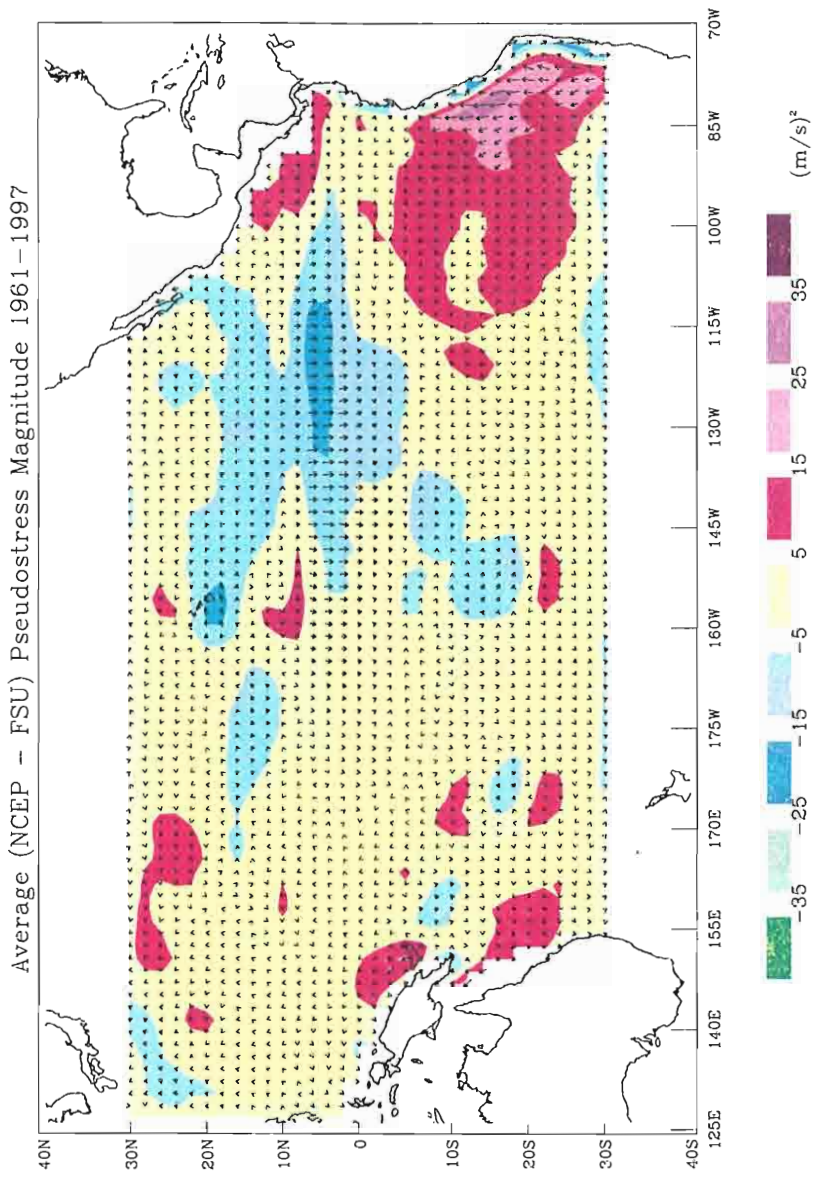


Figure 1: Average magnitude of the NCEP reanalysis pseudostress minus the average magnitude of the FSU pseudostress, with difference vectors. The averages are over all October values from 1961-1997.

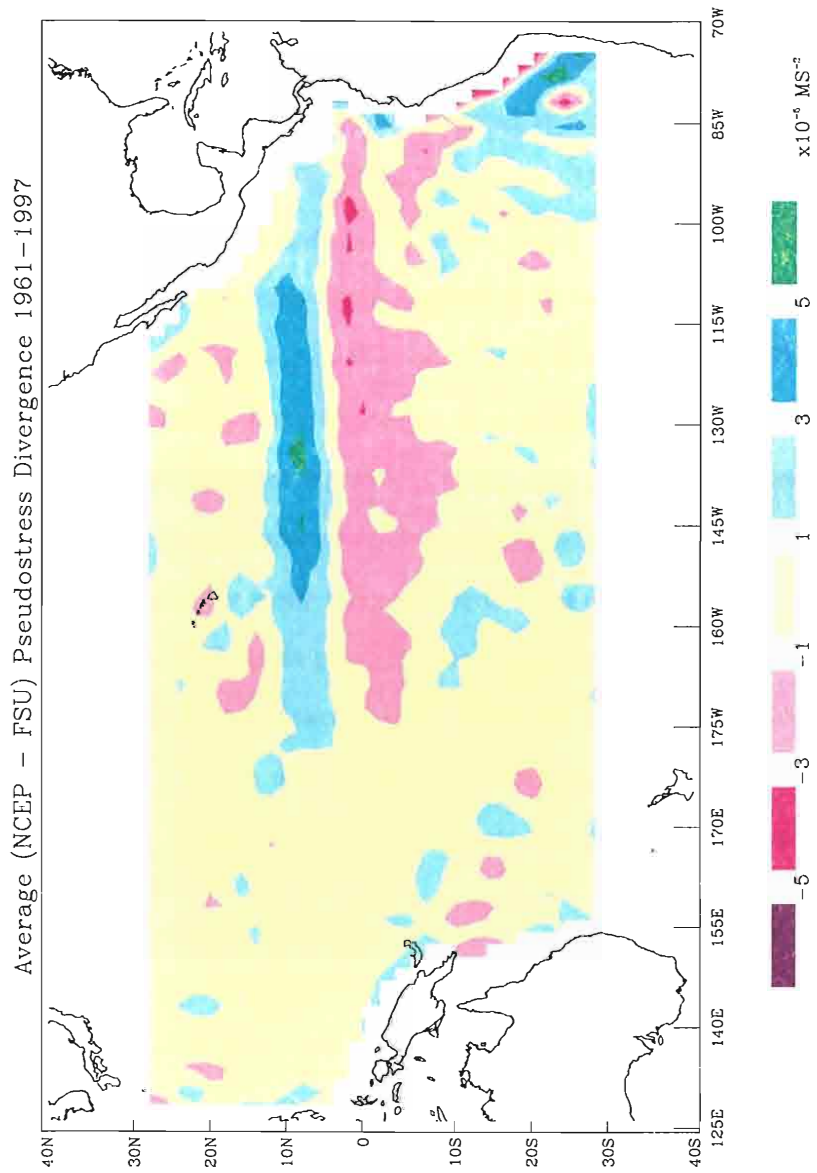


Figure 2: Average divergence of the NCEP reanalysis pseudostress minus the average divergence of the FSU pseudostress. The averages are over all October values from 1961-1997.

2.3 UWM/COADS Climatology

The Comprehensive Ocean-Atmosphere Data Set(COADS) provides monthly mean fields of surface marine climate data for the years 1945-1989, including u and v wind components. Biases in COADS wind measurements result from the use of an old Beaufort equivalent scale for estimating wind speeds based on sea state, and from variations in anemometer heights(*da Silva et al. (1994)*). Wind observations used in the COADS fields are assumed to be recorded at 10 meters, although in many cases ship anemometers range from heights of 15 to 30 meters. The Department of Geosciences at the University of Wisconsin-Milwaukee(UWM) collaborated with the National Oceanographic Data Center to correct the biases in visual observations by determining a new Beaufort equivalent scale. No attempt was made to correct for biases resulting from inconsistent anemometer heights. This collaboration lead to the UWM/COADS monthly mean summaries(*da Silva et al. (1994)*).

The UWM/COADS fields provide monthly mean u and v wind components on a 1° by 1° grid. We have extracted these fields for the Pacific region (40°S to 40°N, 125°E to 70°W). These u and v wind components are converted to monthly mean pseudostress (Eqs. 1 and 2) and then bilinearly interpolated onto the NCEP Gaussian grid.

3. METHODOLOGY

The desired product of this study is a combination of the FSU, NCEP reanalysis, and UWM/COADS pseudostress in smooth realistic fields of monthly mean pseudostress from 1961 to 1997. A simple method would be to piece together the desired FSU region of data with the desired NCEP reanalysis region of data and then interpolate (smooth) along the borders. This is a very primitive method which would lead to inaccuracies in the kinematic fields along the borders of the FSU and NCEP reanalysis data due to large discrepancies between the two datasets (Fig. 1). The method of direct minimization provides an elegant means of blending the desired fields while maintaining realistic physical characteristics in kinematic fields such as divergence and curl (*Legler et al. (1989)*).

The direct minimization technique combines desired fields of data in a nonlinear least-squares problem. The heart of this problem is the cost function to be minimized, which is designed according to the solution field desired. For this study, the cost function includes weighted misfit constraints for the FSU and NCEP reanalysis datasets, and Laplacian, divergence and curl constraints which are intended to impose UWM/COADS climatology information on the solution fields. Each constraint of the cost function is weighted with a spatially dependent coefficient which controls the impact on the solution fields. The result is a smoothed solution field combining the desired features of each dataset as dictated by the cost function.

The direct minimization procedure is applied in this study to combine the best features of the FSU, NCEP reanalysis, and UWM/COADS datasets. The cost func-

The direct minimization procedure is applied in this study to combine the best features of the FSU, NCEP reanalysis, and UWM/COADS datasets. The cost function is weighted with the regional strengths and weaknesses of each dataset in mind.

Kinematic terms are included to insure smoothness of the output magnitude, divergence, and curl fields. The following subsections will describe the details of the cost function, its minimization, and the sensitivity analysis performed to determine the optimal weights for each of the kinematic terms.

The resulting fields provide a robust blend of pseudostress for both tropical and extratropical regions of the Pacific Ocean. The latitudinal extent of these resulting fields lends itself nicely to a study of the relationship between tropical and extratropical pseudostress. Therefore, our study provides a look into this latitudinal relationship on interannual time scales through a complex empirical orthogonal function(CEOF) analysis of the minimization results over the Pacific Ocean from 40° S to 60° N.

3.1 The Cost Function

The cost function to be minimized, F , is designed to combine the strengths of each dataset into a smooth pseudostress field

$$\begin{aligned}
F = & \sum_{x,y} \alpha_{x,y} (\boldsymbol{\tau} - \boldsymbol{\tau}_{FSU})^2 + \sum_{x,y} \beta_{x,y} (\boldsymbol{\tau} - \boldsymbol{\tau}_{NCEP})^2 \\
& + L^4 \sum_{x,y} \gamma_{x,y} [\nabla^2 (\boldsymbol{\tau} - \boldsymbol{\tau}_c)]^2 \\
& + L^2 \sum_{x,y} \Theta_{x,y} [\nabla \cdot (\boldsymbol{\tau} - \boldsymbol{\tau}_c)]^2 \\
& + L^2 \sum_{x,y} \lambda_{x,y} [\hat{\mathbf{k}} \cdot \nabla \times (\boldsymbol{\tau} - \boldsymbol{\tau}_c)]^2
\end{aligned} \tag{3}$$

where $\boldsymbol{\tau}$ is the vector form of the solution pseudostress, $\boldsymbol{\tau}_{FSU}$ and $\boldsymbol{\tau}_{NCEP}$ are respectively the FSU and NCEP reanalysis pseudostress vectors, and $\boldsymbol{\tau}_c$ is the climatology pseudostress vector. Each of the kinematic terms are multiplied by a power of the length scale L ($L = 1^\circ$ latitude) such that all terms of F are dimensionally uniform. The coefficients $\alpha_{x,y}$, $\beta_{x,y}$, $\gamma_{x,y}$, $\Theta_{x,y}$, and $\lambda_{x,y}$ are the spatially dependent weights, specified a priori, which control the influence each term has on the determined $\boldsymbol{\tau}$. Selection of these coefficients are discussed in section 4.2.

The function F determines how the solution pseudostress will be influenced by each dataset. Selection of these coefficients are discussed in section 4.2.

The function F determines how the solution pseudostress will be influenced by each dataset. The first two terms of F represent the misfit of the FSU and NCEP fields with

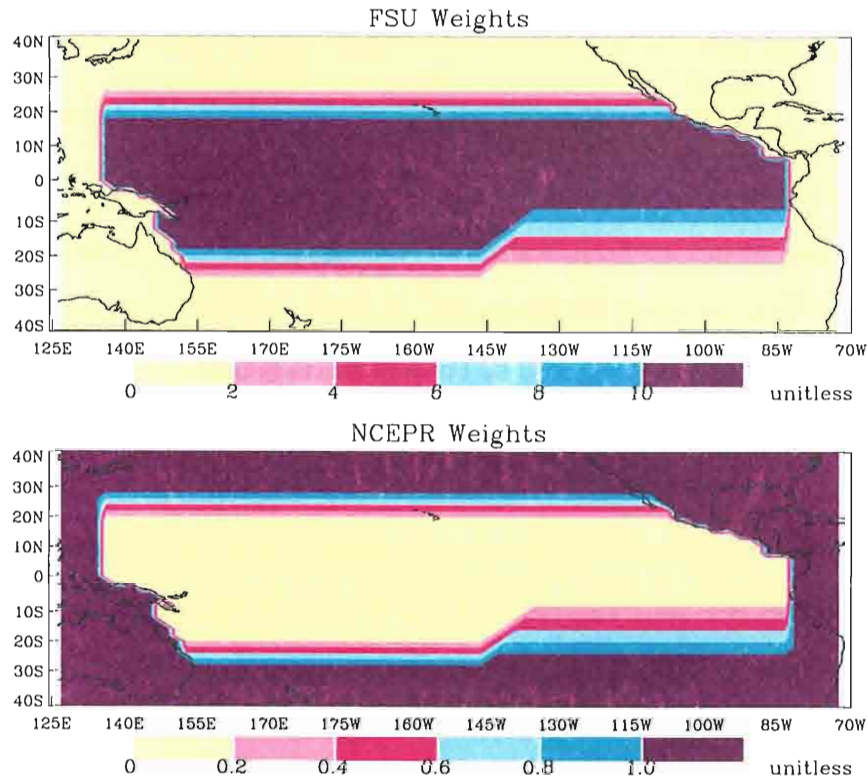


Figure 3: Spatial distribution of weights in the cost function for the FSU constraint, $\alpha_{x,y}$ (top), and the NCEP constraint, $\beta_{x,y}$ (bottom). These are the weights selected a priori according to the desired region of influence for each data set. Note the difference of the scales; the FSU scale is 10 times that of the NCEP reanalysis.

respect to the solution pseudostress. These terms have different spatially dependent weighting functions subjectively determined based on each dataset's strengths and weaknesses as described in section 2 (Fig. 3). These weights define the regional impact of the FSU and NCEP data on the final solution. The third term of F is the Laplacian or smoothing term. This term smooths the the input field according to the climatology field. These first three constraints have a direct impact on the solution vector field.

The fourth and fifth terms of F are kinematic constraints which indirectly impose climatological information on the output. These terms smooth, slightly, the

The fourth and fifth terms of F are kinematic constraints which indirectly impose climatological information on the output. These terms smooth, slightly, the

divergence and curl of the solution field. The degree to which these kinematic fields influence the solution is determined by the selection of the $\Theta_{x,y}$ and $\lambda_{x,y}$ weights.

3.2 Minimization with the Conjugate-Gradient Method

The conjugate-gradient method has been shown to be the optimal method which minimizes a cost function in a large-scale variational analysis (Navon and Legler (1987)). The subroutine CONMIN applies the Shanno (1978) Beale restarted limited-memory quasi-Newton conjugate-gradient method as described in Shanno and Phua (1980). The subroutine CONMIN is used for the minimization in this large-scale assimilation procedure.

The conjugate-gradient method is an iterative method requiring an initial guess field, a cost function, and the gradient of that cost function. For this study, the initial guess field (τ) is a rough combination of the FSU and NCEP pseudostress fields. The fields are simply pieced together and smoothed along the border with a weighted interpolation

$$\tau = \begin{cases} 1.0 \times \tau_{FSU} + 0.0 \times \tau_{NCEP} & \text{if } \alpha_{x,y} = 10 \\ 0.8 \times \tau_{FSU} + 0.2 \times \tau_{NCEP} & \text{if } \alpha_{x,y} = 8 \\ 0.6 \times \tau_{FSU} + 0.4 \times \tau_{NCEP} & \text{if } \alpha_{x,y} = 6 \\ 0.4 \times \tau_{FSU} + 0.6 \times \tau_{NCEP} & \text{if } \alpha_{x,y} = 4 \\ 0.2 \times \tau_{FSU} + 0.8 \times \tau_{NCEP} & \text{if } \alpha_{x,y} = 2 \\ 0.0 \times \tau_{FSU} + 1.0 \times \tau_{NCEP} & \text{if } \alpha_{x,y} = 0 \end{cases} \quad (4)$$

based on the weights (Fig. 3). This eliminates areas in the initial guess where the FSU and NCEP data differ dramatically causing problems for the minimization subroutine.

The subroutine CONMIN requires code to compute the gradient of the cost function F. The cost function and its gradient are written in finite difference form in spherical coordinates. The gradient of the cost function is used to find the search direction for the minimization. At times the conjugate-gradient method can produce improper search directions. In this case the CONMIN subroutine applies the Beale restart method (Beale (1972)) which updates the search direction when the minimize improper search directions. In this case the CONMIN subroutine applies the Beale restart method (Beale (1972)) which updates the search direction when the min-

imization is not converging. Iterations are stopped when the norm of the gradient is reduced by 1.5×10^{-2} .

The Shanno limited-memory quasi-Newton method and the Beale restart method are described in detail in *Navon and Legler (1987)*.

3.3 CEOF Analysis

Prior to this study, a robust dataset did not exist for studying the interannual relationship between tropical and extratropical surface pseudostress. The results of the blended FSU and NCEP pseudostress fields provide a more complete representation of the entire Pacific basin to study decadal variability. Empirical orthogonal function (EOF) analysis has been used to study the interannual variability of sea surface temperature (SST) (*Tourre and White (1995)*), and other scalar fields. Vector fields can be analyzed in a similar manner using complex empirical orthogonal function (CEOF) analysis (*Horel (1984)*).

CEOF analysis is applied to the resulting blended fields in this study to determine the relationship between tropical and extratropical regions on interannual time periods. Before the CEOF analysis is performed, the monthly mean climatologies, created from the solution fields, are removed from the pseudostress data, and the data are filtered in time with an 18-month low-pass Kaylor filter (*Kaylor (1977)*). CEOF analysis, also called complex principle component analysis, requires the vector field be broken into a real part, the u-component, and an imaginary part, the v-component. A complex covariance matrix is formed from the complex data, and normalized by the number of stations analyzed. In this case, 3911 grid points were analyzed from January 1962 through December 1996, a total of 419 months. Due to the large latitudinal extent of this dataset, 40° S to 60° N, the filtered anomalies scaled by the cosine of the latitude (*Tourre and White (1995)* and *North et al. (1982)*). This scaling eliminates the geometrical effects of the grid spacing which results from the increasing cosine of the latitude (*Tourre and White (1995)* and *North et al. (1982)*). This scaling eliminates the geometrical effects of the grid spacing which results from the increasing area of grid boxes at higher latitudes. This is necessary in order to study the variance

throughout the domain independent of the grid. The eigenvalues and eigenvectors of the covariance matrix are calculated. The eigenvectors are then used to create spatial functions from the data using the following relationship

$$\mathbf{S}_N(i) = \sum_{n=1}^{nt} \tau_N(i, n) \mathbf{E}_N(n). \quad (5)$$

Where \mathbf{S} is the spatial function, τ is the blended data, \mathbf{E} is the eigenvector, i is the station index from 1 to 3911, and n is the time index from 1 to 419. There are 419 spatial functions, represented by N . Each spatial function represents a certain percent of the variance as quantified by the relative value of the eigenvalues.

The results are analyzed by studying the time series of the eigenvectors in the form of an amplitude and a rotation angle. The real part of the eigenvectors determines the amplitude and the imaginary part controls the rotation angle. The eigenvectors and spatial functions are studied to reveal the interannual variability of the blended fields for eigenvalues which represent a significant amount of the variance.

4. RESULTS

4.1 FSU and NCEP Weight Selection

The weights $\alpha_{x,y}$ and $\beta_{x,y}$ are selected a priori based on the known characteristics of the FSU and NCEP datasets (Fig. 3). The FSU weight dominates from 20° S to 20° N, where the FSU weight is set to 10.0 and the NCEP weight is zero, with the exception of the southeast corner of this region. The corner of this region is where the FSU fields rely on sparse numbers of observations. Therefore, the weights impose a stronger influence from the NCEP data in this corner. The transition zones of the two datasets are smoothed by a gradual change in the weights from 0.0 to their maximum value. This transition is over a 10 degrees latitude distance, between 20° and 30° both north and south, except the southeast corner. The southeast corner has a transition over 15 degrees latitude, between 10° S and 25° S. The larger transition zone accommodates for the dramatic differences between the two datasets in this region, which requires a more gradual smoothing. The $\alpha_{x,y}$ and $\beta_{x,y}$ weights denote the region of influence each data set has on the blended solution.

The magnitude of the first weight, $\beta_{x,y}$, is arbitrarily selected to have a maximum of 1.0. The NCEP weight decreases by 0.2 evenly through the transition zone described above. The FSU weight is selected to be 10 in the equatorial regions and decrease evenly by 2 through the transition zones. This is done to compensate for the FSU region being ‘sandwiched’ in between the NCEP region of influence. Due to this ‘sandwiched’ effect, information from the NCEP region will spread into the FSU region as a result of the finite differencing in the cost function. The $\alpha_{x,y}$ weight must be increased to bring back the FSU information in the final solution.

4.2 Sensitivity Results

The weights, $\gamma_{x,y}$, $\Theta_{x,y}$, and $\lambda_{x,y}$ are subjectively chosen parameters which can have a significant impact on the solution fields. Optimal values for these parameters are not easily defined. Analysis of the sensitivity of these parameters, the change in the solution per change in the parameter, provides further insight in selecting optimal values for these weights (Meyers *et al.* (1994)). We will follow this approach. Changes in the solution fields are studied by defining response functions which are typically integrated measures of the solution fields. The response functions used are the magnitude, divergence, and curl of the resulting fields. Each of the weights are varied individually and their impact on the three response functions are analyzed using sensitivity plots. Sensitivity is presented as plots of the response function for a given longitude band versus the weight value. Many such analyses were completed, only a few are presented here.

A weight is determined to be highly sensitive if small changes in the weight produce large changes in the response function, hence solution fields. Small changes in a weight with weak sensitivity produce small changes in the response function. Weights with weak sensitivity and a small impact on the response function can have large values as dictated by the sensitivity plots. The final weights are chosen such that each term has a significant impact on the solution avoiding weights which the sensitivity plots reveal to be highly sensitive.

The following analysis is for the month of August 1991, at the longitude band of 135.0° W. Similar results were obtained for other months. Magnitude is chosen to be the first response function analyzed. The results of the sensitivity analysis with divergence and curl response functions are very similar and will be discussed together.

The Laplacian weight, $\gamma_{x,y}$, has a significant impact on the magnitude response function (Fig. 4). When $\gamma_{x,y}$ is increased to 0.5, the magnitude response is on the

The Laplacian weight, $\gamma_{x,y}$, has a significant impact on the magnitude response function (Fig. 4). When $\gamma_{x,y}$ is increased to 0.5, the magnitude response is on the order of typical pseudostress magnitude fields at $\pm 3.0 m^2 s^{-2}$. As $\gamma_{x,y}$ is increased

above 1.0, the magnitude response is not as sensitive to the weight selection. There is very little change in the magnitude response function as $\gamma_{x,y}$ increases from 1.0 to 12.0. Although the $\gamma_{x,y}$ weight has a large impact on the magnitude response, its sensitivity to changes between 1.0 and 12.0 is weak.

A north-south banding structure is clearly present in the sensitivity plot for the Laplacian weight (Fig. 4). This banding can be explained by the manner in which the Laplacian term smooths the solution. In locations along the 135° W longitude band where the initial guess field has a local maximum, the Laplacian term attempts to smooth this maximum according to the climatology. This smoothing is accomplished by decreasing the values over the maximum, and increasing the values surrounding the local maximum. Therefore, a banding structure is seen in the sensitivity plots such that negative values exist over the local maxima, and positive response values are seen to either side (north and south) of the maxima. Similar north-south banding structures are seen in the divergence and curl response functions described below.

The divergence weight, $\Theta_{x,y}$, has less of an impact on the magnitude response than the Laplacian weight (Fig. 5). There is nearly zero response to increases in $\Theta_{x,y}$ from 0.0 to 1.5. As $\Theta_{x,y}$ is increased above 1.5 an impact on the magnitude response function begins to be seen. However, this impact is on the order of $10^{-2}m^2s^{-2}$, two orders of magnitude smaller than typical pseudostress magnitude fields. When $\Theta_{x,y}$ is increased further, from 6.0 to 12.0, the magnitude response drops to near zero and then increases again. Although the divergence weight is sensitive to small changes in its value, the impact of this weight on the magnitude response function is considerably smaller than that of the Laplacian weight. There is not an obvious region of significant response for this divergence weight.

The curl weight, $\lambda_{x,y}$, behaves similarly to the divergence weight (Fig. 6). It is sensitive to changes in its value between 0.0 and 12.0. However, the impact on the magnitude response function is only on the order of $10^{-2}m^2s^{-2}$. For values of

Magnitude is the Response Function

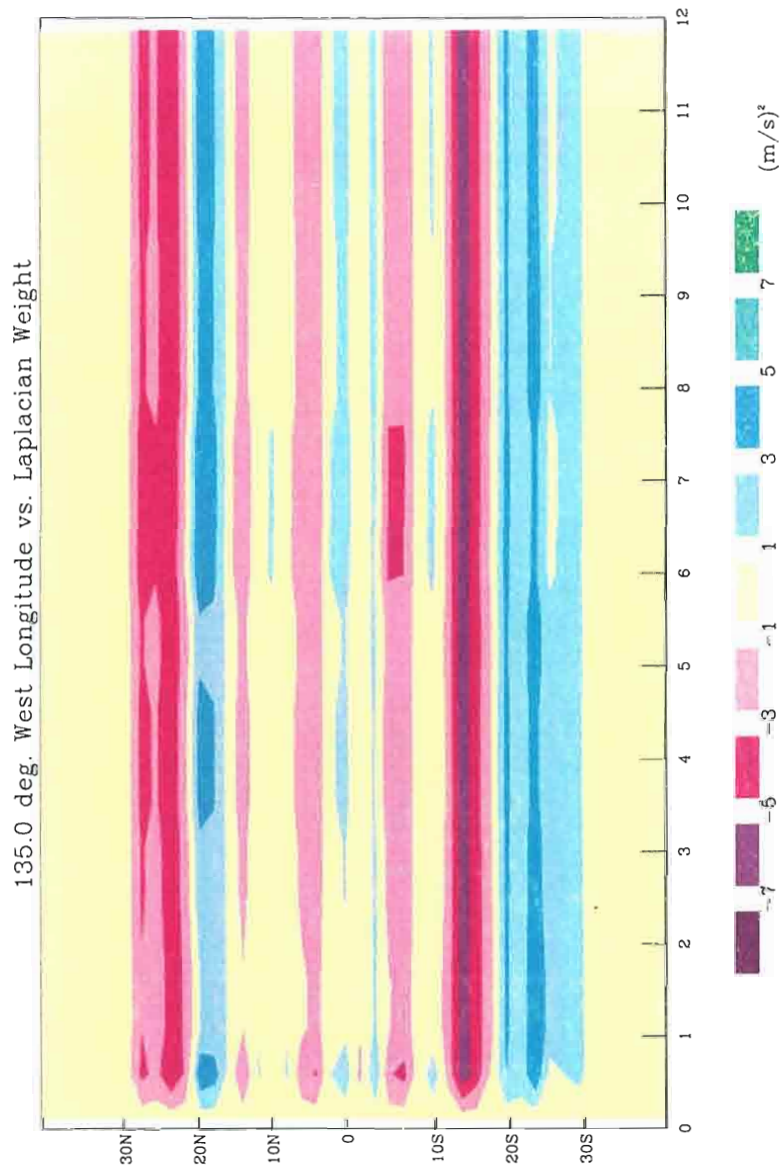


Figure 4: August 1991 pseudostress magnitude response function for the 135° W longitude band as a function of the Laplacian weight. The Laplacian weight is varied from 0.0 to 12.0 in the cost function, keeping all other weights constant at 1.0. The magnitude at each weight is subtracted from the magnitude for a weight of 0.0 to determine the response. Positive values indicate increasing pseudostress magnitude with increasing Laplacian weight.

with increasing Laplacian weight.

Magnitude is the Response Function

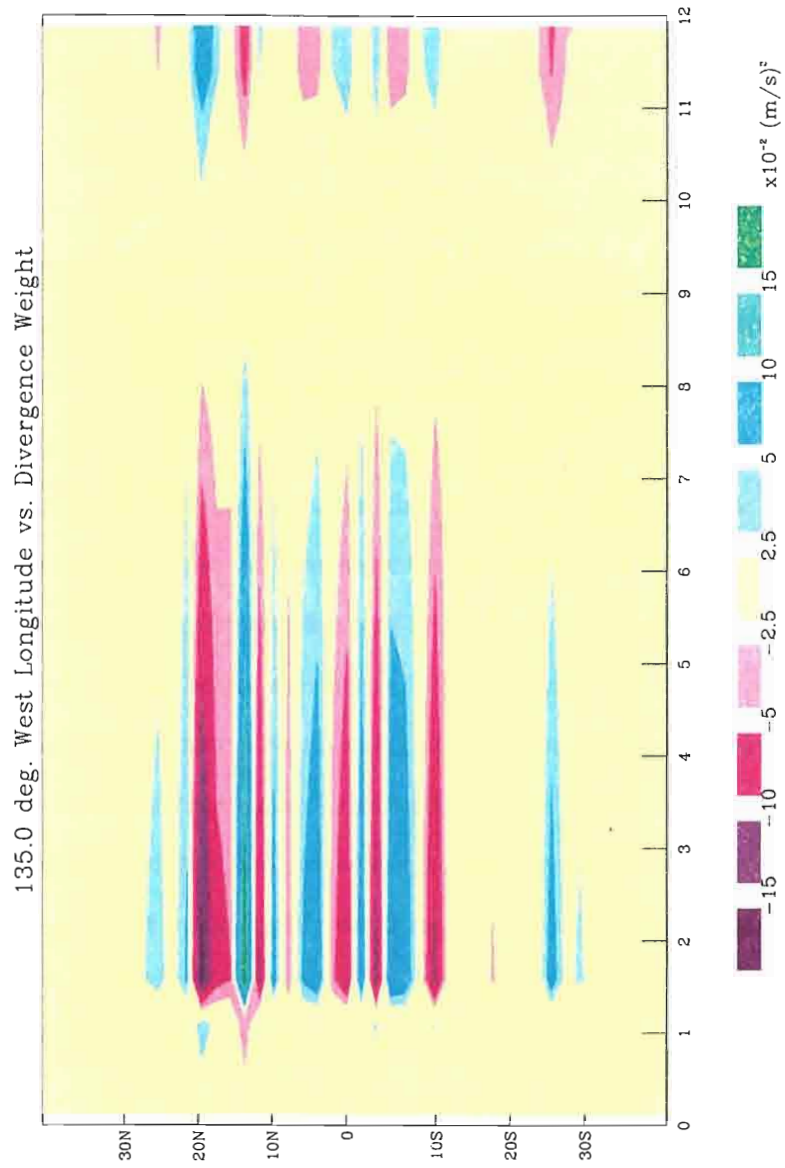


Figure 5: Same as figure 4 except the divergence weight varies from 0.0 to 12.0. Note the scale change such that the response is on the order of 10^{-2} .

$\lambda_{x,y}$ greater than 10.0, there is a more dramatic impact on the magnitude response function. The bands of response broaden and the impact on the magnitude response function increases. The curl weight does not have a significant response until its value is increased above 10.0.

The Laplacian weight has a significant impact on the divergence and curl response functions. Similar to the magnitude response for the Laplacian weight, the divergence response (Fig. 7) increases to $\pm 10^{-5}ms^{-2}$, which is on the order of typical pseudostress divergence fields. The divergence and curl responses are not sensitive to variations in $\gamma_{x,y}$ from 1.0 to 12.0. The divergence and curl responses for the $\Theta_{x,y}$ and $\lambda_{x,y}$ weights are similar to the magnitude response. These weights are both sensitive to variations from 0.0 to 12.0; however, their impacts on the response functions are two orders of magnitude smaller than that of the Laplacian weight.

The optimal values for the kinematic weights are found in regions of the sensitivity plots which are not highly sensitive and also have a noticeable effect on the response functions. Due to the lack of sensitivity in variations of $\gamma_{x,y}$ above a value of 1.0, the Laplacian weight can have a small value and still provide an impact on the solution fields. Because the divergence and curl weights have less of an impact on the response functions than that of the Laplacian weight, it is reasonable to select larger values for $\Theta_{x,y}$ and $\lambda_{x,y}$. By avoiding highly sensitive regions of the sensitivity plots, we avoid selecting a weight which could have an unwanted impact on the resulting solution. Therefore, we look for regions in the sensitivity plots which reveal a constant response. The $\lambda_{x,y}$ weight provides a constant response above 10.0 (Fig. 6). This response is also the most significant response $\lambda_{x,y}$ imposes on the solution. Therefore, $\lambda_{x,y}$ is selected to be 11.0 in the middle of this constant response region. $\Theta_{x,y}$ does not reveal an obvious region of constant response. A value of 9.5 is chosen, and the impact on the solution fields is studied in the remainder of this section.

The values of the smoothing and kinematic weights selected above are held constant and the impact on the solution fields is studied in the remainder of this section.

The values of the smoothing and kinematic weights selected above are held con-

Magnitude is the Response Function

135.0 deg. West Longitude vs. Curl Weight

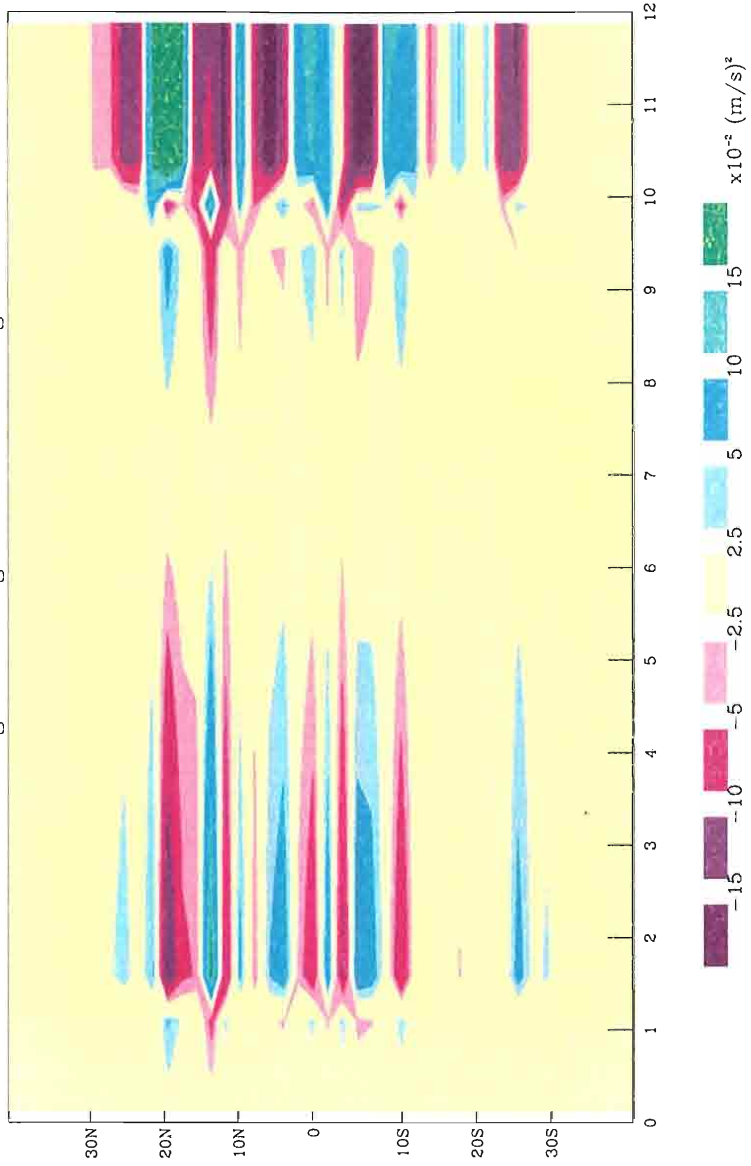


Figure 6: Same as figure 4 except the curl weight varies from 0.0 to 12.0.

Divergence is the Response Function

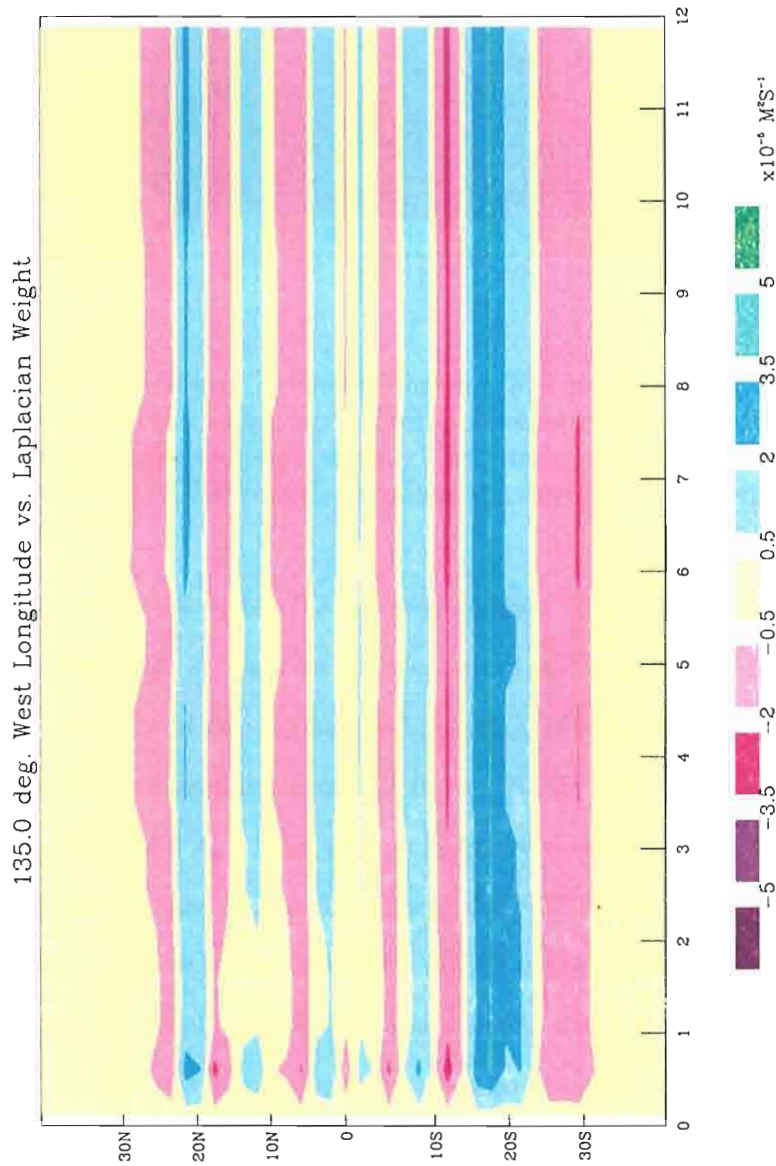


Figure 7: August 1991 pseudostress divergence response function for the 135° W longitude band as a function of the Laplacian weight. The Laplacian weight is varied from 0.0 to 12.0 in the cost function, keeping all other weights constant at 1.0. The divergence at each weight is subtracted from the divergence for a weight of 0.0 to determine the response. Positive values indicate increasing divergence (decreasing convergence) with increasing Laplacian weight.

convergence) with increasing Laplacian weight.

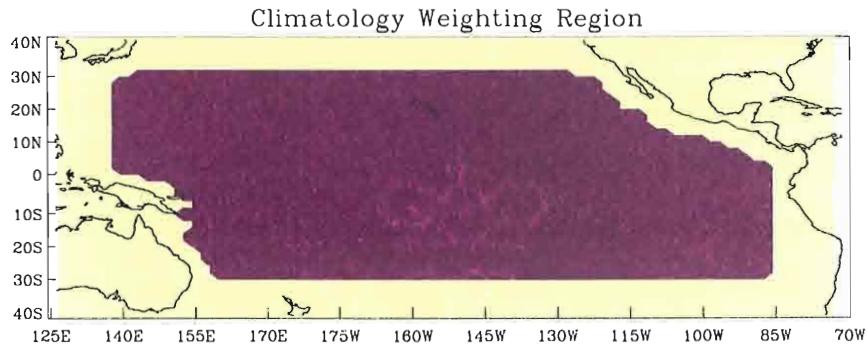


Figure 8: The climatology weighting region. The purple region denotes the area in which the misfit to climatology values are evaluated in the cost function for the Laplacian, divergence, and curl terms. The remaining region denotes the area in which the misfit to NCEP reanalysis values are used for the kinematic terms of the cost function.

stant for all grid points within the analysis domain. Within the selected climatology weighting region (Fig. 8), the cost function analyzes the misfit of the analysis to the climatology. Outside of this region the Laplacian, divergence, and curl terms of the cost function are analyzed using misfits to the NCEP reanalysis data with the same weights, $\gamma_{x,y}$, $\Theta_{x,y}$, and $\lambda_{x,y}$. This is done to insure that the values at the edges of the blended analysis domain do not differ from the NCEP reanalysis values. Thus, the blended analysis can be inserted into the NCEP reanalysis to create global fields.

To examine the combined effect of the selected weights, the minimization is performed with each of the kinematic weights set to zero and the resulting analyses are compared to the results of the minimization with the weights set as selected above for a sample month of August 1991. Each of the analyzed fields of magnitude, divergence, and curl reveal the importance of including the kinematic terms in the cost function.

The smoothing and kinematic terms have the largest effect on areas in the analyzed fields of the initial guess which differ dramatically from the climatology. For example, two local maximums exist along the 175° W longitude band south of the equator fields of the initial guess which differ dramatically from the climatology. For example, two local maximums exist along the 175° W longitude band south of the equator for the August 1991 FSU magnitude field (Fig. 9) which, as one would expect, do

not appear in the UWM/COADS climatology. By including the Laplacian term in the cost function with the selected weight, these maxima are smoothed by slightly decreasing the maximum and slightly increasing the surrounding values (Fig. 10). It is acceptable and expected that the solution field will differ greatly from the climatology; the Laplacian term insures that this difference is "smooth". The same effect can be seen for the larger maximum off the coast of New Guinea, around 160° E and 10° S. This maximum is approximately $20 \text{ m}^2\text{s}^{-2}$ greater than the climatology. The smoothing term decreases this maximum by more than $9 \text{ m}^2\text{s}^{-2}$, while at the same time increasing the surrounding values by more than $6 \text{ m}^2\text{s}^{-2}$.

Similar results are found when examining the curl and divergence fields. The ITCZ for August 1991 (Fig. 11) is stronger than the climatology. The kinematic terms act to decrease the convergence along the southern edge of the ITCZ (Fig. 12). At the same time, the kinematic terms increase the convergence north and south of the ITCZ. A slight decrease in the strength of the ITCZ exists in the FSU field at 115° W and 9° N (Fig. 11). The kinematic terms smooth this detail out of the minimization solution by increasing the convergence in this location. In general, the FSU divergence field is more detailed than the smooth climatology field, as expected. This results in smoothing effects on the divergence field throughout the FSU region of influence when the kinematic terms are included in the cost function. Therefore, the FSU region of the minimization solution is a smoothed product of the FSU pseudostress.

In combination, the weights selected based on the sensitivity analysis have a significant impact on the solution fields. The kinematic terms do smooth the divergence and curl of the minimization solution. Thus, including the kinematic weights (Θ, λ) has an impact on the solution for specified values of other weights (α, β, γ) .

4.3 Final Direct Minimization Results

The minimization produces a well-blended product of the FSU and NCEP pseu-

4.3 Final Direct Minimization Results

The minimization produces a well-blended product of the FSU and NCEP pseudostress products according to the spatial dependence of the weighting functions.

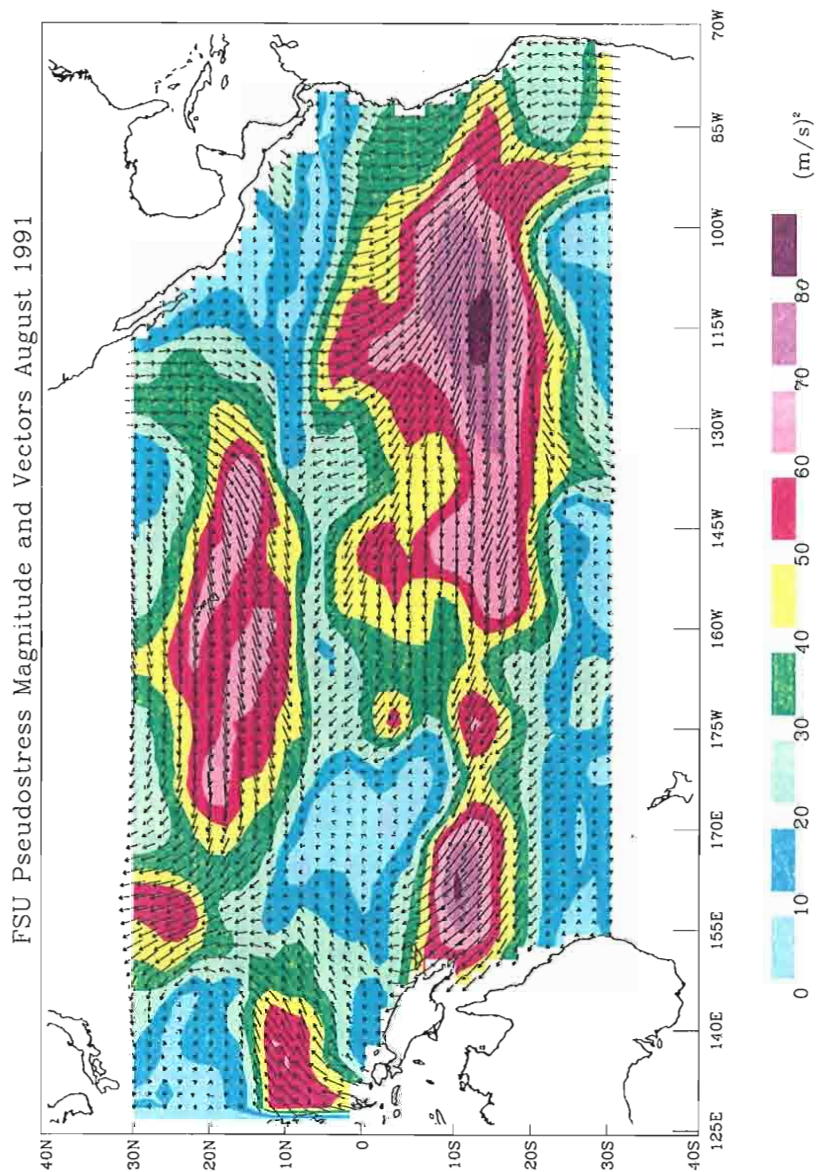


Figure 9: FSU pseudostress magnitude and vectors, August 1991. Note the two local maxima along the 175° W longitude band south of the equator.

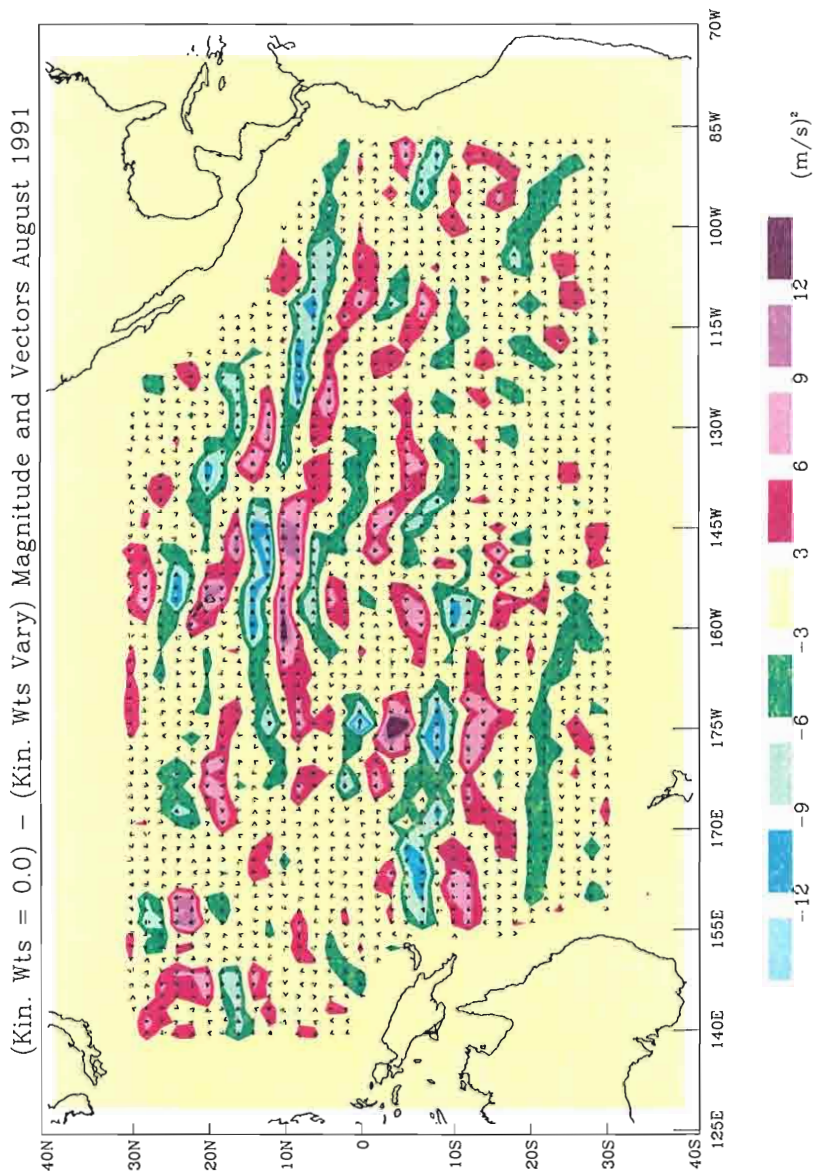


Figure 10: Magnitude of direct minimization solution with kinematic weights set to zero minus the magnitude of the solution with nonzero kinematic weights, $\gamma_{x,y}=1.0$, $\Theta_{x,y}=9.5$, $\lambda_{x,y}=11.0$. Note the significant impact of the kinematic terms along the 175° W longitude band, in the region of the two local maxima seen in the FSU magnitude field (Fig. 9).

magnitude field (Fig. 9).

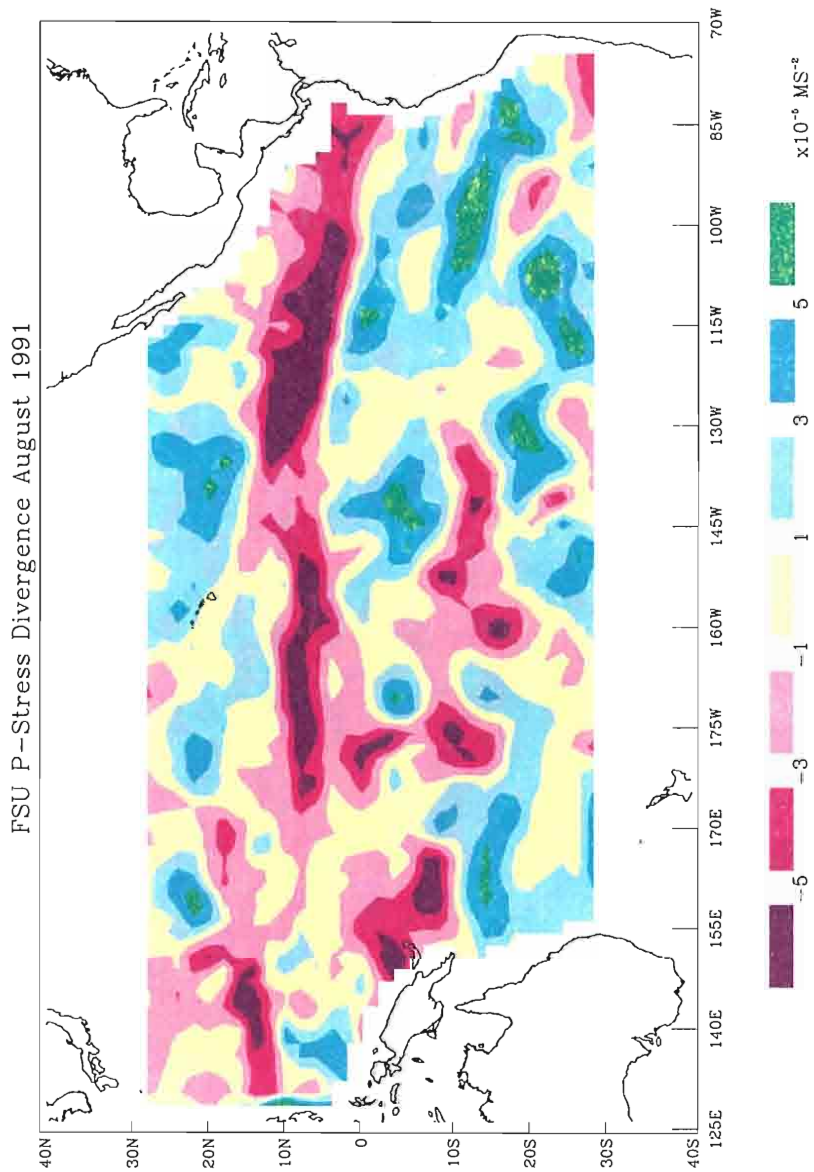


Figure 11: FSU pseudostress divergence, August 1991. Note the position of the ITCZ around 10° N. Negative values indicate horizontal convergence.

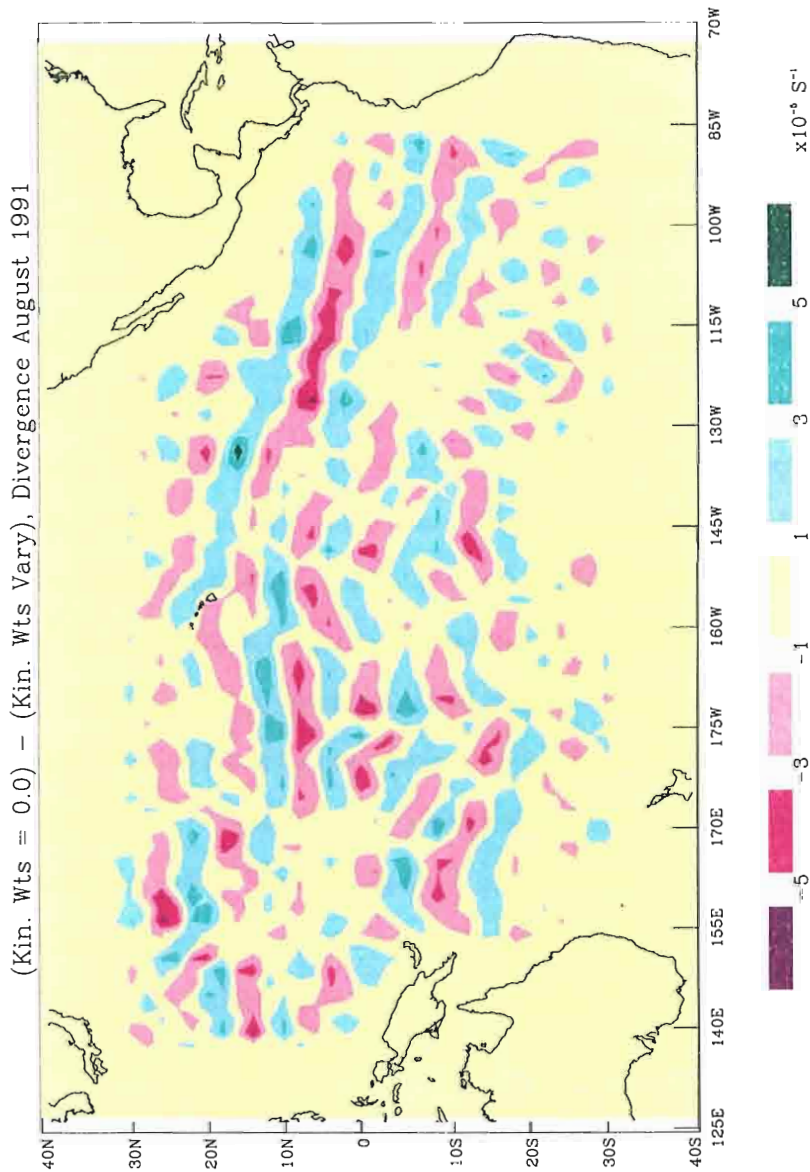


Figure 12: Divergence of direct minimization solution with kinematic weights set to zero minus the divergence of the solution with nonzero kinematic weights, $\gamma_{x,y}=1.0$, $\Theta_{x,y}=9.5$, $\lambda_{x,y}=11.0$. Note the significant impact of the kinematic terms along the ITCZ. The ITCZ is positioned along the 10° N latitude band (Fig. 11). Positive (negative) values indicate increased (decreased) convergence when the Laplacian and kinematic weights are non-zero.

kinematic weights are non-zero.

Continuing to use August 1991 as an example, the difference between the magnitude of the minimization result (Fig. 13) and the magnitude of the NCEP reanalysis clearly reveals the presence of the weighting function (Fig. 14). The largest differences between these two fields occur over the FSU region of influence. The northeast and southeast trades are stronger in the minimization solution as dictated by the FSU term in the cost function. The transition zones are the site of a gradual decrease in the differences to exactly zero difference around the border of the analysis domain. Because these differences are exactly zero around the border, the minimization result can easily be inserted into the global NCEP reanalysis field without generating any artificial noise in the derivative fields around the border of our domain.

The effects of the spatially dependent weighting function can also be seen in the difference of the minimization result with respect to the FSU pseudostress magnitude (Fig. 15). There are large differences between the two fields in the southeast corner where the NCEP weighting dominates the result. As expected, the southeasterlies off the coast of South America are stronger in the minimization solution than that of the FSU analysis. The smoothing and kinematic terms have a significant impact on the resulting field within the FSU region of influence (Fig. 15). These smoothing and kinematic terms smooth the local extremes as described in the sensitivity analysis results. Clearly, the minimization solution has been blended as expected, retaining the dominant features of the FSU and NCEP magnitude fields in the desired regions, while smoothing the result based on the climatology.

The successful application of the spatially dependent weighting to the minimization solution for all of the analyzed months is studied by looking at the impacts for a given longitude band, 135° W. It is obvious that the weighting function is properly applied such that the difference between the magnitude of the minimization solution and the magnitude of the NCEP reanalysis is largest in the FSU region of influence and gradually decreases through the transition zones to exactly zero (Fig. solution and the magnitude of the NCEP reanalysis is largest in the FSU region of influence and gradually decreases through the transition zones to exactly zero (Fig.

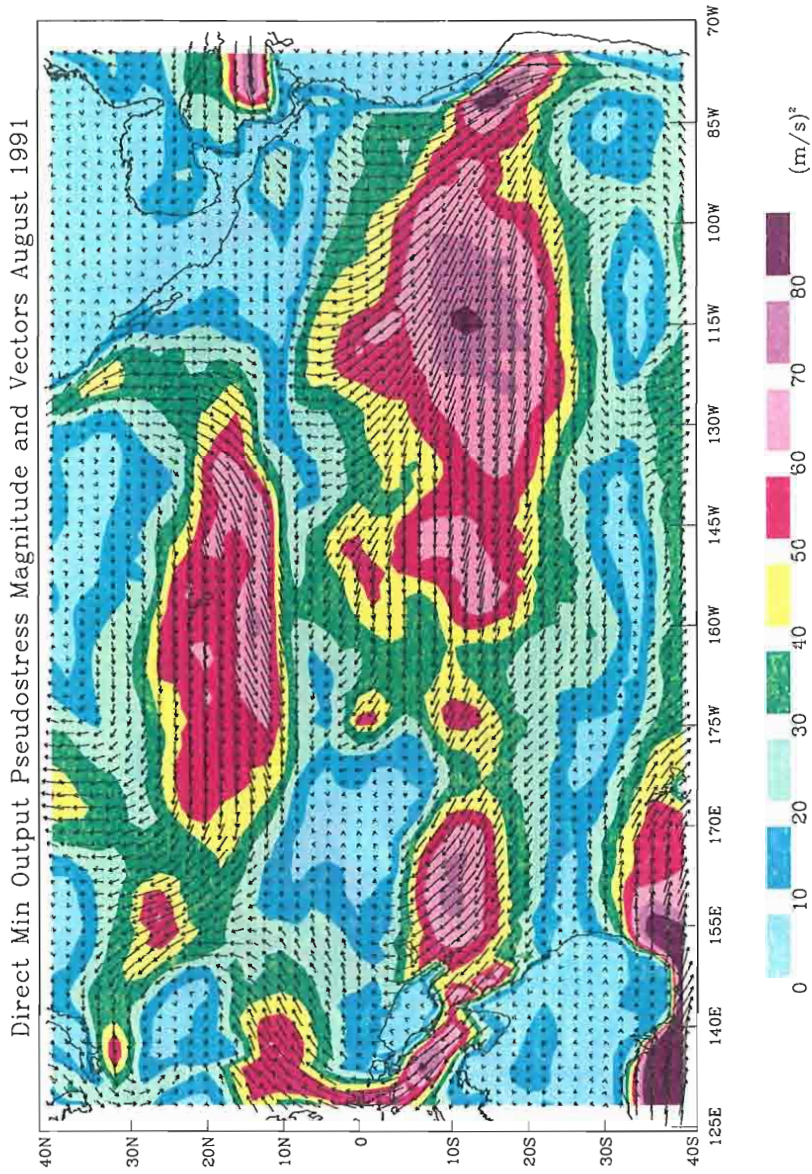


Figure 13: Magnitude of the minimization solution pseudostress with vectors, for August 1991.

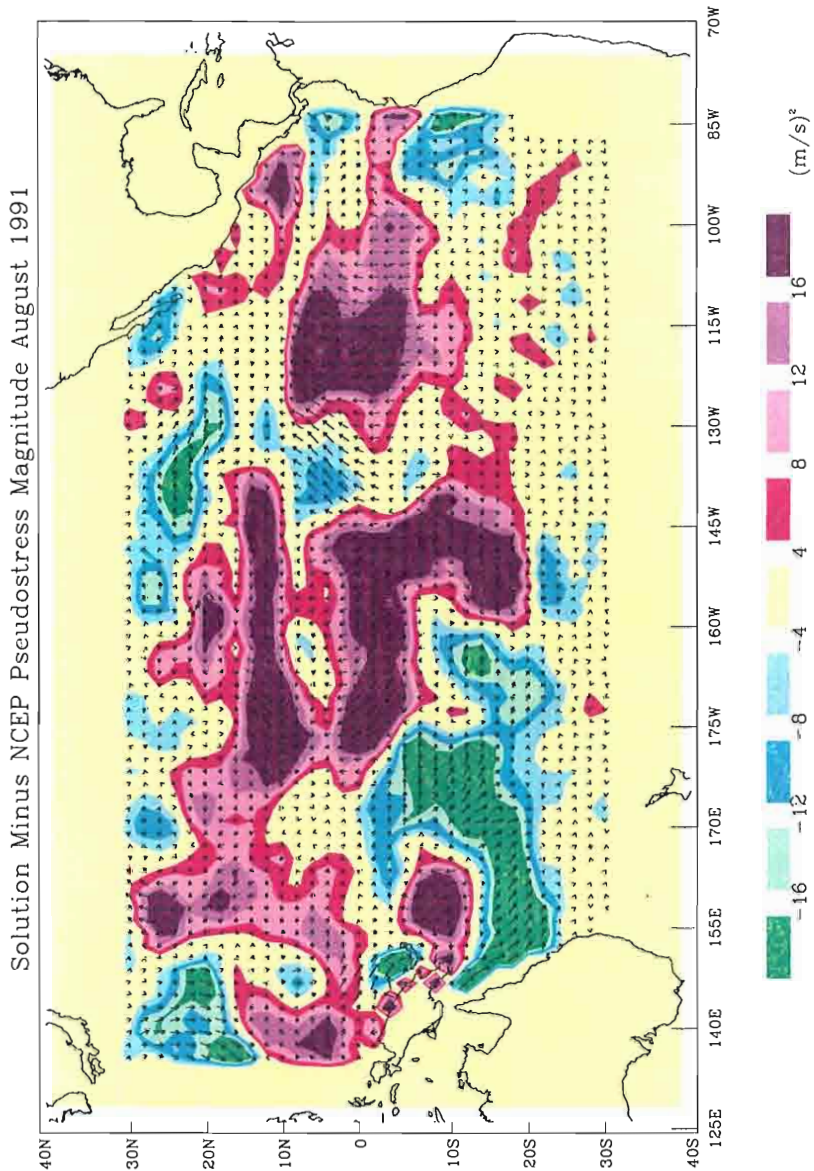


Figure 14: Magnitude of the minimization solution pseudostress minus the magnitude of the NCEP pseudostress with difference vectors, for August 1991. The surrounding yellow region of the domain which is void of vectors is exactly zero. Note the large differences in the FSU region of influence, and the gradual decrease in the differences through the transition zones.

through the transition zones.

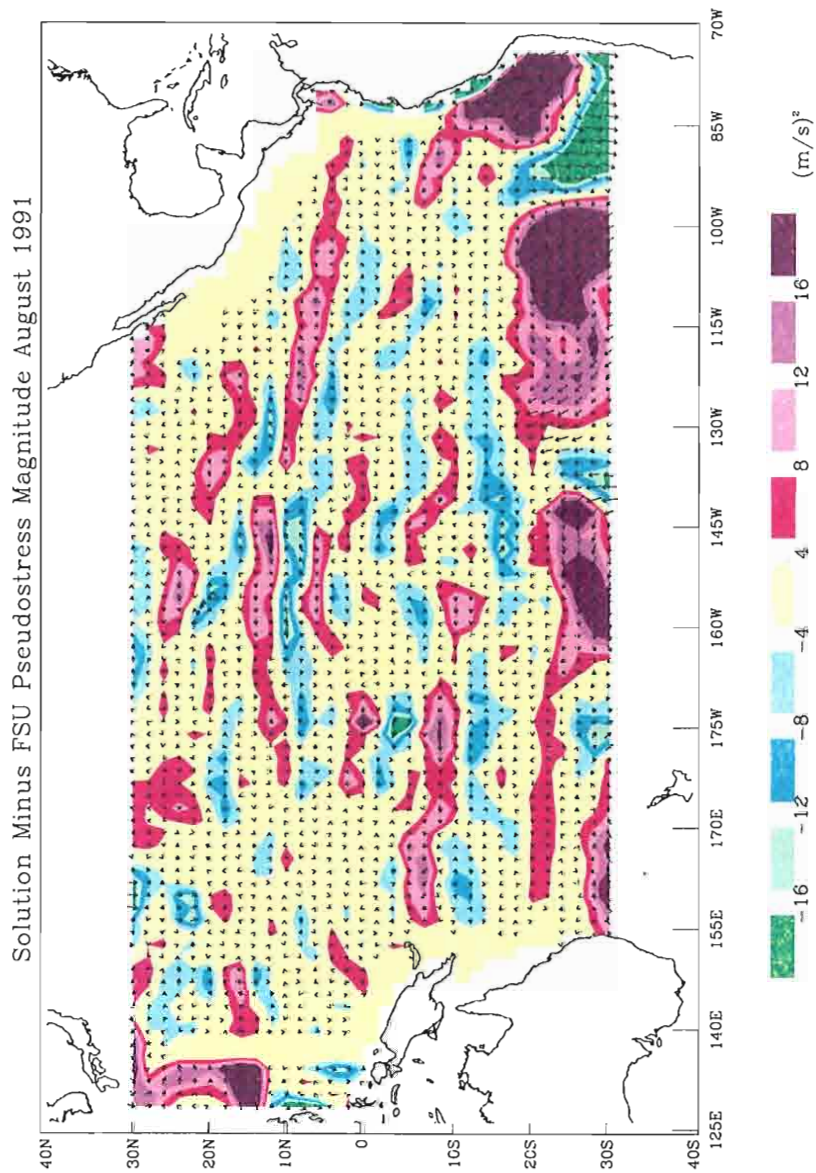


Figure 15: Same as figure 14, except the difference is with respect to FSU pseudostress magnitude. Large differences exist where the NCEP weight dominates. The differences in the FSU region of influence are a result of the inclusion of the kinematic terms in the cost function.

16). Notice that the difference values change sign such that it appears as though the minimization output increases in magnitude as compared to the magnitude of the NCEP reanalysis. It is a good assumption, based on the design of the cost function, that the minimization solution in the FSU region is a smoothed version of the FSU pseudostress product (Fig. 17). The sign change we observe may be explained by an increase in magnitude of the FSU winds beginning in the late 1970's. This increase in magnitude is possibly a result of a failure to compensate for changes in the ship anemometer heights, or it is simply a matter of the natural variability of the wind. A strong scientific conclusion based on one longitude band is not possible. Further examination of this sign change is required outside of this study.

The minimization result provides a different representation of the ITCZ, which is faint to nonexistent in the NCEP reanalysis field (Fig. 18). The ITCZ is stronger in the minimization solution than it is in the NCEP reanalysis (Fig. 18). This is a result of the stronger northeast and southeast trades in the solution field increasing the convergence as compared to that of the NCEP reanalysis. This result is consistent for all months of the analysis (Fig. 19). It is interesting to note that the sign change observed in the magnitude difference for the NCEP reanalysis (Fig. 16), does not appear to influence the divergence difference. The smoothing and kinematic terms do smooth the ITCZ, as well as other extreme features of the initial guess field, as dictated by the climatology. Along the ITCZ the smoothing and kinematic terms reduce the convergence, while increasing the convergence north and south of the ITCZ in the initial guess fields (Fig. 20), providing further evidence of the north-south banding pattern seen in the sensitivity plots. The derivative fields of the minimization result maintain the physical properties of the FSU and NCEP analyses as desired.

4.4 CEOF results

Once the variational blending has been applied to each month of the 37 year analysis,

4.4 CEOF results

Once the variational blending has been applied to each month of the 37 year analysis, from 1961 through 1997, the NCEP reanalysis 10-meter pseudostress from 40° N

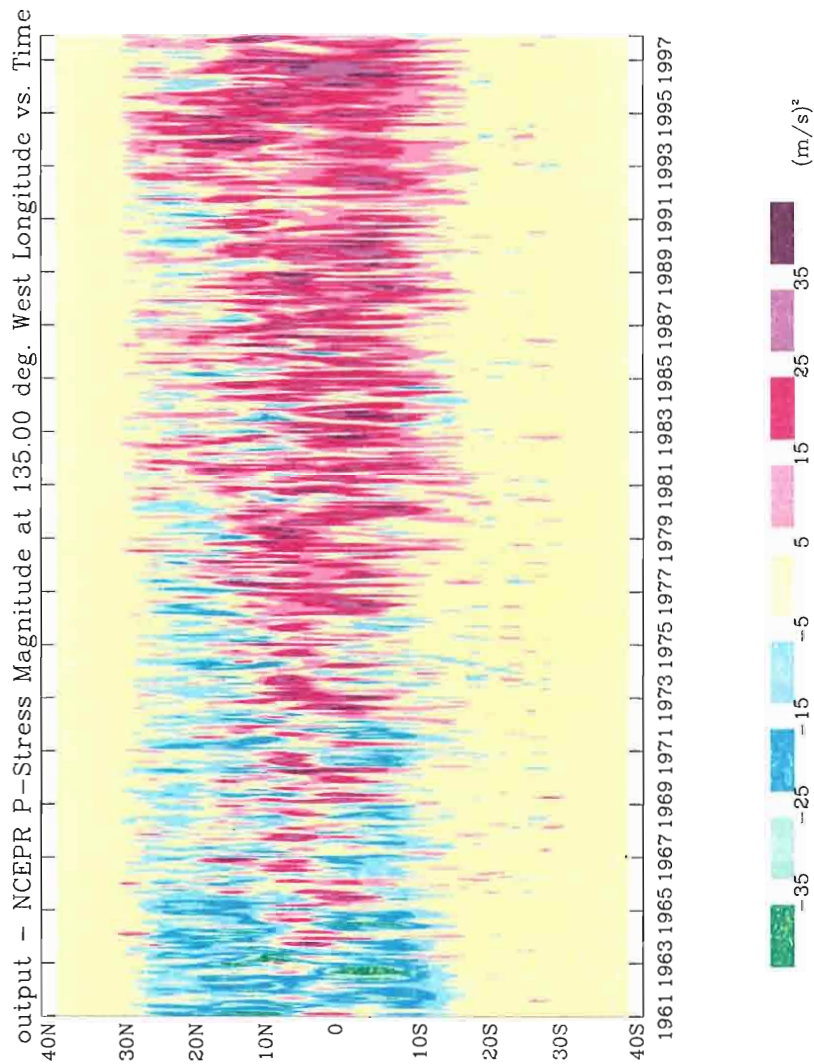


Figure 16: Magnitude of the minimization solution pseudostress minus the magnitude of the NCEP reanalysis pseudostress along the 135° W longitude band versus time. The Largest differences are located in the FSU region of influence, 15° S to 30° N. The differences gradually decrease to zero through the transition zones.

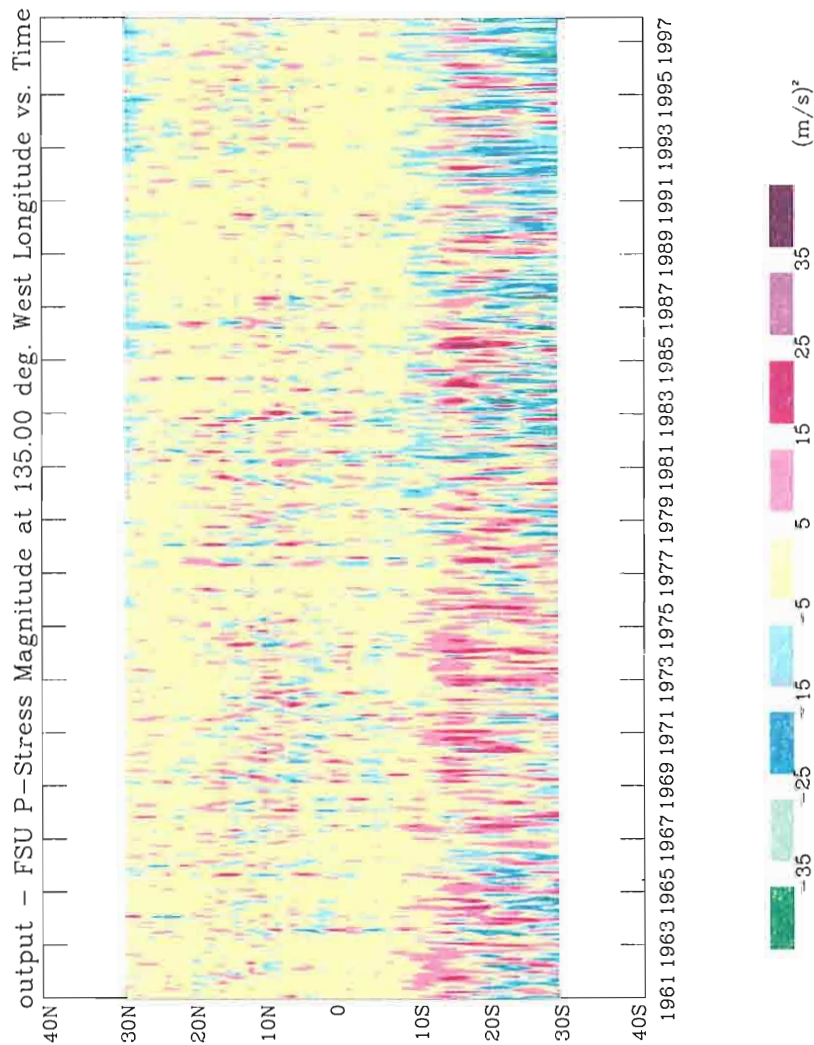


Figure 17: Same as figure 16, except the difference is with respect to FSU pseudostress magnitude. Note the consistency of the impact of the weighting function through time with the largest differences below 10° S in the NCEP region of influence. Also, the effects of the kinematic terms are consistent through time within the FSU region of influence. Thus, the FSU region of the minimization solution is a smoothed product of the FSU pseudostress.

of the FSU pseudostress.

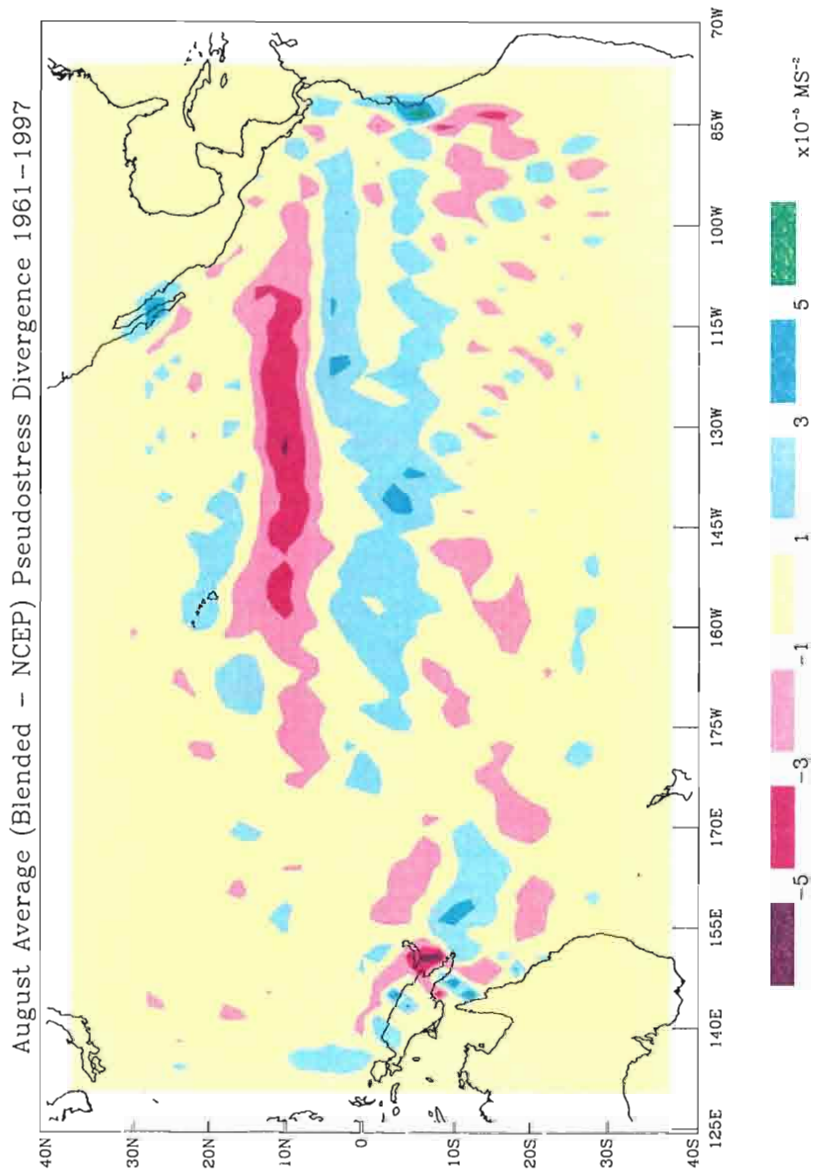


Figure 18: Average divergence of the minimization solution pseudostress minus the average divergence of the NCEP reanalysis pseudostress, average of August values from 1961-1997. Note the large differences along the ITCZ (Fig. 11), where the output field has stronger convergence than the NCEP field.

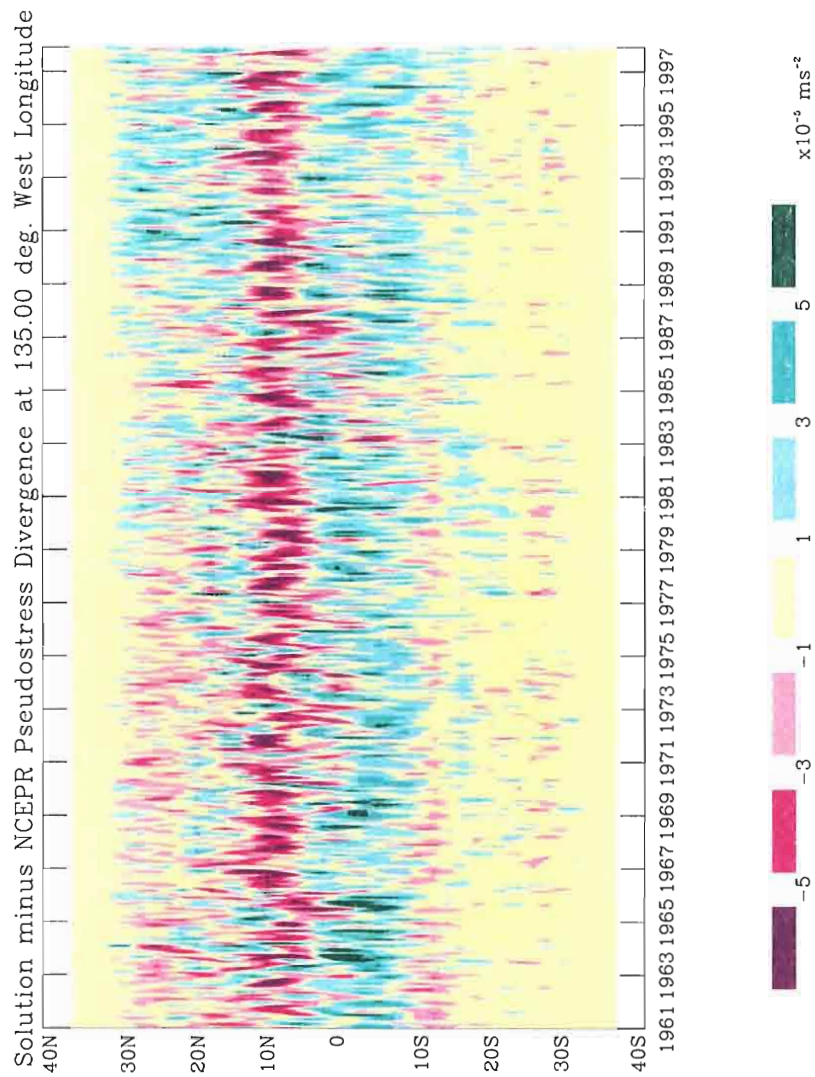


Figure 19: Divergence of minimization solution pseudostress minus the divergence of the NCEP pseudostress along the 135° W longitude band versus time. Note the stronger convergence in the minimization solution between 5° N and 15° N which results from a stronger ITCZ in the divergence of the minimization result.

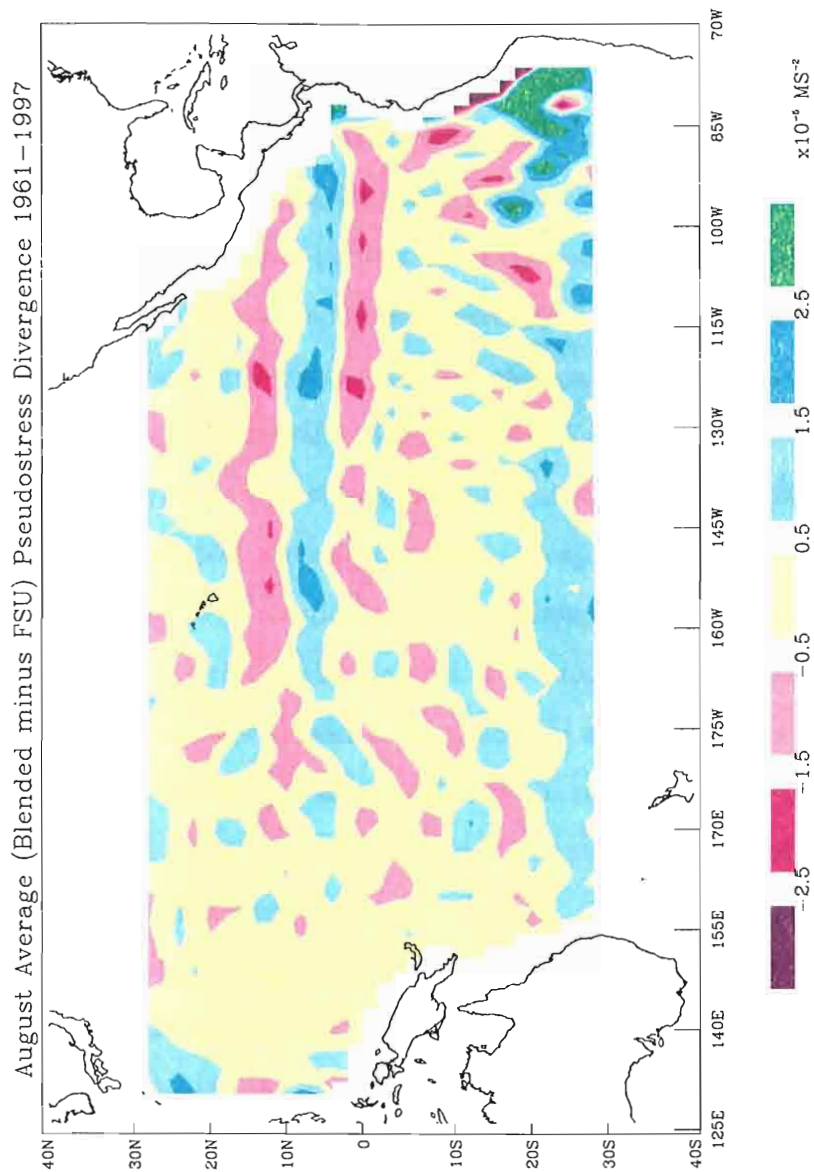


Figure 20: Same as figure 18 except the difference is with respect to FSU pseudostress divergence. The largest differences appear in regions where the NCEP weight dominates. The kinematic terms in the cost function have the largest effect along the ITCZ, climatologically located just south of the 10° N latitude band.

to 60° N are added to the northern edge of the domain such that we can examine variability over a larger latitudinal extent. Because our approach forces the blended fields to be the NCEP reanalysis solution at our boundaries, adding the global NCEP fields to our blended fields is seamless. The monthly mean climatologies, calculated from the new blended product, are removed, and each data point is filtered in time with an 18-month low-pass Kaylor filter (*Kaylor (1977)*). This allows us to look at variability on interannual time periods. A CEOF analysis (*Legler (1983)*) is performed on this new analysis domain of filtered anomalies. The CEOF analysis results in 419 spatial functions and eigenvectors (principal components), each representing a certain percent of the spatio-temporal variance as determined by the eigenvalues. A scree test (*Wilks (1995)*) is used to determine which principal components are statistically significant. The complex eigenvectors (time series) are expressed here as amplitude and rotation angle. The rotation angle represents the counterclockwise rotation of each of the vectors in the spatial function. The product of a spatial function and its corresponding eigenvector creates a time series of spatial patterns accounting for a certain percent of the variance as quantified by the relative value of the corresponding eigenvalue. The sum of the product of every eigenvector and spatial function will recreate the original dataset.

The following subsections will break down the details of the first four spatial functions and eigenvectors, cumulatively accounting for 51 percent of the variance. In general, the most significant time periods for each of the eigenvectors occur with approximately a 90° or 270° counterclockwise rotation of the vectors in the spatial functions; our description of the spatial patterns will focus on patterns with these rotation angles. Finally, the sequence of events for various El Niño and El Viejo years will be discussed focusing on the role each eigenvector plays in the development, maturation, and dissipation of each event, and the extratropical response in the North Pacific. These sections provide a look at the similar characteristics of the various maturation, and dissipation of each event, and the extratropical response in the North Pacific. These sections provide a look at the similar characteristics of the various

ENSO events, as well as the variability from one event to another.

The First Principal Component

The first spatial function (Fig. 21) represents 22.76 percent of the variance. Rotating the vectors of the first spatial function 90° counterclockwise, this spatial pattern represents the classic El Niño anomalous westerlies in the western equatorial Pacific (*Rasmusson and Carpenter (1982)*). The northeast and southeast trade anomalies are oriented equatorward with northerly flow across the normal position of the ITCZ as described in (*Rasmusson and Carpenter (1982)*). The maximum convergence and strongest anomalies appear south of the equator around 3° S from 170° E to 150° W. This portion of the CEOF pattern agrees with the mature phase of the canonical El Niño anomaly composite as described in *Rasmusson and Carpenter (1982)*. The pattern off the coast of South America from 30° S to 15° S extending out to 110° W is not consistent with the results of *Rasmusson and Carpenter (1982)*. This region shows anomalous north-westerlies in our analysis, which is opposite of the anomalies seen in *Rasmusson and Carpenter (1982)*. The striking presence of a strengthening of the Aleutian low, centered near its climatological position at 50° N and 167° W, accompanies this typical mature phase El Niño signal. The strengthening of the Aleutian low during El Niño winters (December-February) has been observed in geopotential height fields (*Horel and Wallace (1981)*), as well as model derived height fields over the North Pacific (*Lau (1997)*). These observations are consistent with our analysis. There also appears to be a cyclonic anomaly in the southwest Pacific over New Zealand.

The amplitude and rotation angles (Fig. 22) reveal the details of the spatio-temporal variability of this spatial function. This eigenvector is clearly in phase, from 1970-1997, with the SST anomalies in the equatorial Pacific as defined by the Japan Meteorological Agency (JMA) index (based on monthly mean SST anomalies averaged 1970-1997, with the SST anomalies in the equatorial Pacific as defined by the Japan Meteorological Agency (JMA) index (based on monthly mean SST anomalies averaged for the area 4° N to 4° S and 150° W to 90° W). The peaks of amplitude for the

El Niño years of 1973, 1983, 1987, and 1992 are each accompanied by rotation angles around 90° . The 1973, 1983, and 1992 peaks occur from December-February (labeled by the year during which the January and February fall); the 1987 peak occurs later in the year from January-June. The 1983 peak possesses the largest amplitude, while the 1987 event spans the longest duration. Previous work has examined the variability of SST anomalies as it relates to ENSO (*Tourre and White (1995)*). Each of the amplitude peaks for the first eigenvector are coincident with the peak SST anomalies in the central equatorial pacific, which also agrees with the mature phase anomaly composite of *Rasmusson and Carpenter (1982)*. The El Niño years in the 1960's (1963, 1965, and 1969) exhibit smaller amplitudes and do not appear as prominent periods for this eigenvector, it is interesting to note that this period is also out of phase with the JMA index.

The years of 1971, 1974, 1976, and 1988 are represented by a 270° counterclockwise rotation of the first spatial function (Fig. 21) coincident with amplitude peaks, from December-February, in the first eigenvector. These peaks occur in phase with the negative values of the JMA index (Fig. 22), denoting an El Viejo year (the cold phase of ENSO). The spatial pattern for these time periods is dominated by easterly anomalies in the equatorial Pacific, strengthened southeast trades, along with a weakening of the Aleutian low, centered near its climatological position.

The Second Principal Component

The second CEOF spatial function (Fig. 23), representing 11.16 percent of the variance, has its largest response associated with the Aleutian Low. With a 90° counterclockwise rotation of this spatial function, the Aleutian Low is weakened and shifted southeast of its normal position to 155° W and 48° N. There is significant northeasterly flow associated with the Aleutian Low through the 30° N longitude band from 170° E to 145° W. North of the equator up to 10° N from 140° E to 160° W, easterly flow associated with the Aleutian Low through the 30° N longitude band from 170° E to 145° W. North of the equator up to 10° N from 140° E to 160° W, there are anomalous westerlies. This pattern appears the winter-spring before the

moderate to strong El Niños of 1969, 1973 and 1983 (Fig. 24), preceding the JMA index positive SST anomaly peaks; this is slightly lagged with respect to the findings of *Emery and Hamilton* (1985) in which seasonal mean atmospheric sea level pressure charts showed a weakened Aleutian Low the winter before the 1973 and 1983 El Niño events. This pattern also appears coincident with the weak El Niño event of 1966 (Fig. 24).

When the second spatial function is rotated 270° the Aleutian Low is strengthened, and there are easterly anomalies present north of the equator in the western Pacific. This occurs after the peak phase of the 1983 El Niño and less significantly after the peak phase of the 1973 El Niño event (Fig. 24). This pattern slowly decreases in amplitude through the weakening phases of the 1983 event, as the anomalies return to easterlies over the western equatorial Pacific and the strength of the Aleutian Low diminishes. This pattern also precedes the El Viejo events of 1971, 1974, 1976, and 1988 (negative peaks in the JMA index) by 3-4 months.

The Third Principal Component

The third CEOF spatial function, representing 10.01 percent of the variance, shows significant values east of the dateline just south of the equator (Fig. 25). These anomalies are northwesterly stretching from 160° W to 100° W. Southwesterly anomalies are seen in the region of the northeast trades, just south of Hawaii, indicating these trade winds are weakened. This pattern appears during the 1983 event after the mature phase (Fig. 26); this agrees with the findings of *Rasmusson and Carpenter* (1982) who found that westerly anomalies do not appear in the eastern equatorial Pacific until 2-3 months after the positive sea surface temperature anomalies peak during the mature phase. This pattern is also dominant during the weak El Niño events of 1963, 1966, and 1969 (Fig. 26), preceding SST anomaly peaks in the JMA index by 6-8 months. Recalling the lack of significance the first principal El Niño events of 1963, 1966, and 1969 (Fig. 26), preceding SST anomaly peaks in the JMA index by 6-8 months. Recalling the lack of significance the first principal component revealed during these events, this is an interesting finding that the third

component peaks as a precursor to the positive SST anomalies prior to 1970.

The third principal component does not appear significant during El Viejo events other than the 1988 event (Fig. 26). During this event, southeasterly anomalies are present in the eastern equatorial Pacific, along with strengthened northeast trades, from January through September of 1988. This event will be described in greater detail later in this section. The third eigenvector is relatively unimportant throughout the 1970's.

The Fourth Principal Component

The fourth principal component, representing 7.02 percent of the variance, also links the equatorial anomalies with the Aleutian low (Figs. 27 and 28). Although the scree test does reveal this component to be statistically significant, it is important to note that the largest magnitudes of the anomalies associated with the fourth component (the product of the amplitude of the eigenvector and the magnitude in the spatial function) is never greater than $12m^2s^{-2}$, which is relatively small compared to the other principal components.

Anomalies in the western equatorial Pacific, north of the equator are easterly when the spatial function (Fig. 27) is rotated 90° counterclockwise. This is coincident with westerly anomalies in the eastern equatorial Pacific, south of the equator, with the strongest anomalies centered around 135° W and 4° S. The Aleutian low is weakened and shifted south and east of its normal position. This pattern appears in the latter stages (February-July) of the El Niño events in our analysis, with the exception of the 1969 and 1992 events. In combination with the second principal component, the fourth component represents the dissipation of the westerly anomalies in the western equatorial Pacific, and a decrease in the strength of the Aleutian low.

When rotated 270° counterclockwise, the pattern reverses. Westerly anomalies are found in the western equatorial Pacific, north of the equator, and easterly anomalies

When rotated 270° counterclockwise, the pattern reverses. Westerly anomalies are found in the western equatorial Pacific, north of the equator, and easterly anomalies spread across the southern edge of the equator from 155° W to 115° W. The Aleutian

low is strengthened and remains shifted south and east of its typical location. This pattern occurs 10-12 months prior to the El Niño events of 1969, 1983, and 1987. We also note this pattern appearing in 1995-1996.

The 1982-83 El Niño Event

The 1982-83 El Niño event is marked by westerlies in the western equatorial Pacific, north of the equator, and a weakening of the northeast trades. The second and fourth eigenvectors (modes) represent this development phase of the El Niño (Figs. 29 and 30). Westerly anomalies develop in the western equatorial Pacific (160° E to 160° W, 10° N to 2° S) from January through April of 1982 (second and fourth modes). These westerly anomalies become southwesterly anomalies as they approach 160° W where they represent a weakening of the northeast trades. Easterlies remain present in the eastern and central equatorial Pacific (160° W to 100° W, 10° S to equator). SST anomalies begin to increase slightly in the central equatorial Pacific; at the same time, the Aleutian low is weakened and northeasterly flow from 20° N to 40° N and 140° W to 160° E, associated with the weakened low, feeds into the westerly anomalies (second mode). Through the summer months of 1982, westerly anomalies begin to develop further east along the equator, remaining west of 150° W (the second and fourth modes begin to diminish as the first mode grows in amplitude).

Moving into the fall of 1982, the El Niño begins to mature (the first mode begins to peak). Westerly anomalies begin to spread east across the equator and become northwesterly around 150° W. Easterly anomalies remain along the equator, east of 120° W. The Aleutian low begins to strengthen in November through January (the first mode peaks in mid-January and the second and fourth modes dissipate). Coincident with the first mode peak, SST anomalies peak for the first time along the equator with the largest SST anomalies extending from the coast of Peru out to 140° W. The anomalies north of the equator in the central Pacific are northly, the equator with the largest SST anomalies extending from the coast of Peru out to 140° W. The anomalies north of the equator in the central Pacific are northly, and converge into the region of the largest SST anomalies (the first mode peak).

After the first SST anomalies peak, northwesterly anomalies develop in the eastern equatorial Pacific crossing the equator and extending to 5° S (third mode peak in late February and early March of 1983). Moving into April and May of 1983, northwesterly anomalies develop in the eastern tropical Pacific, and the strengthened Aleutian low is shifted south and east of its typical position, now centered at 150° W and 45° N, and northeasterly anomalies appear east of 160° E, north of the equator (first mode dissipates, and modes two and four begin to rise for a second time with rotation angles of 270° counterclockwise). As the northwesterly anomalies strengthen in the eastern equatorial Pacific in May and June of 1983, the SST anomalies peak for a second time; this SST anomaly peak occurs along the coast of Peru stretching along the equator out to 95° W.

The El Niño begins to dissipate as easterly anomalies return in the western equatorial Pacific from 160° W to 140° E in June and July of 1983 (second and fourth mode peaks). By July of 1983, easterly anomalies begin to return throughout the western equatorial Pacific and the northeast trades begin to strengthen (the first and third modes have decreased in amplitude considerably, and the second and fourth modes dominate). Northwesterly anomalies remain south of the equator in the eastern Pacific (fourth mode). Into the fall of 1983, the equatorial anomalies are returning to normal, and the strength of the Aleutian low diminishes as the El Niño event of 1982-83 comes to an end (second and fourth modes diminish).

The 1972-73 El Niño Event

A similar sequence of events occurs during the 1972-73 El Niño (Figs. 31 and 32). Each of the amplitudes are considerably lower during this event, especially the first mode peak which is approximately half the size of its peak during the 1982-83 event. The developmental stages of this event are nearly identical to that of the 1982-83 event with westerlies developing just north of the equator in the western Pacific, The developmental stages of this event are nearly identical to that of the 1982-83 event with westerlies developing just north of the equator in the western Pacific, and a weakened Aleutian low during the winter and spring of 1972. Changes in the

sequence of events begin to appear during the mature phase (the first mode peak is smaller in amplitude than that of the 1983 event). This peak still occurs during December and January of the El Niño year, coincident with the SST anomalies peak along the equator in the central and eastern Pacific. Westerly anomalies occur in the eastern tropical Pacific south of the equator from January through April (fourth mode). March through July of 1973 mark the development of easterlies in the western equatorial Pacific, north of the equator (fourth and second modes). The third mode never enters the picture in this event.

Beginning in August of 1983, signs of the 1973-74 El Viejo setting up appear as southeasterly anomalies begin to spread into the central equatorial Pacific and the Aleutian low weakens (the first mode increases at a rotation angle approaching 270°). The Aleutian low continues to weaken into January of 1974 as the SST anomalies become negative, and the El Viejo continues to develop. The rapid shift into an El Viejo event may be the cause of the variations from what was seen during the 1982-83 event.

The El Niño Events of the 1960's

Although the sequence of events were quite similar for the 1972-73 and 1982-83 El Niño events, other years produced dramatically different time series in the CEOF analysis. The El Niños of the 1960's (1963, 1965, and 1969) are coincident with relatively small amplitudes for the first mode (Fig. 22). These years are represented by the second through fourth modes. The 1965 event begins with a weakening of the northeast and southeast trades (third mode) in December of 1964 through March of 1965 (Figs. 33 and 34). Northwesterly anomalies develop in the eastern equatorial Pacific south of the equator from 150° W to 115° W, extending southward to 10° S. Through the summer of 1965, the northeast trades are strengthened and westerly anomalies spread into the central equatorial Pacific (second mode). The Aleutian S. Through the summer of 1965, the northeast trades are strengthened and westerly anomalies spread into the central equatorial Pacific (second mode). The Aleutian low weakens and westerly anomalies strengthen in the central and eastern Pacific just

south of the equator from October through November of 1965 (second and fourth modes). These anomalies occur 1-3 months after a peak in the SST anomalies from October through November. These SST anomalies peak two to three months earlier than what was observed for the strong events of 1973 and 1983, and dissipate rapidly during the early months of 1966. The westerly anomalies dissipate in the tropical Pacific through the spring of 1966 (second and fourth modes dissipate).

Modeling results have shown that the El Niños of the 1960's are a result of the cessation of the normal semiannual variability of the central Pacific easterlies, rather than an anomalous relaxation of the easterlies (*Busalacchi and O'Brien* (1981)). This conclusion provides an explanation for the relatively small amplitudes observed in the first mode during these events; this normal semiannual variability will not appear in the filtered pseudostress fields. Therefore the anomalous relaxation of the westerlies in the central equatorial Pacific, represented by the first mode, will not appear as a significant peak during these events. It is also noted by *Busalacchi and O'Brien* (1981) that the 1963 El Niño is only influenced by variability east of the dateline. Our analysis supports this conclusion, as the third mode is the only significant amplitude peak contributing to the variability during this event (Figs. 35 and 36), representing westerly anomalies in the eastern equatorial Pacific, and a weakening of the northeast trades.

The 1988-89 El Viejo Event

The El Viejo event of 1988-89 begins in the winter of 1988 with easterly anomalies appearing south of the equator in the eastern Pacific (third mode) (Figs. 37 and 38). The northeast trades over and south of Hawaii strengthen. Moving into June and July of 1988, the Aleutian low slightly strengthens and easterly anomalies develop in the western equatorial Pacific north of the equator (second mode). The SST anomalies reach a negative peak from August of 1988 through January of 1989 (in between peaks western equatorial Pacific north of the equator (second mode). The SST anomalies reach a negative peak from August of 1988 through January of 1989 (in between peaks of the first and second modes). Strong southeasterly anomalies across the equator

and throughout the central equatorial Pacific occur coincident with a weakening of the Aleutian low into the winter of 1988 (modes two and three diminish, and the first mode begins to increase into November and December).

The equatorial easterly anomalies begin to diminish in the spring of 1989 (first mode dissipates). Easterly anomalies persist and then dissipate south of the equator in the eastern Pacific toward the end of the event from June to November (third mode), along with the return to normal of the Aleutian low (first mode decreases considerably). Each of the first three modes contribute to easterly anomalies in the equatorial Pacific throughout this event. The fourth mode does not enter into this event remaining relatively small in amplitude throughout this period.

Other El Viejo events occur during the 1960's and 1970's (1964, 1967, 1970, 1973, and 1976). The first mode represents the peak phases for each of these events with little contribution from the other three modes.

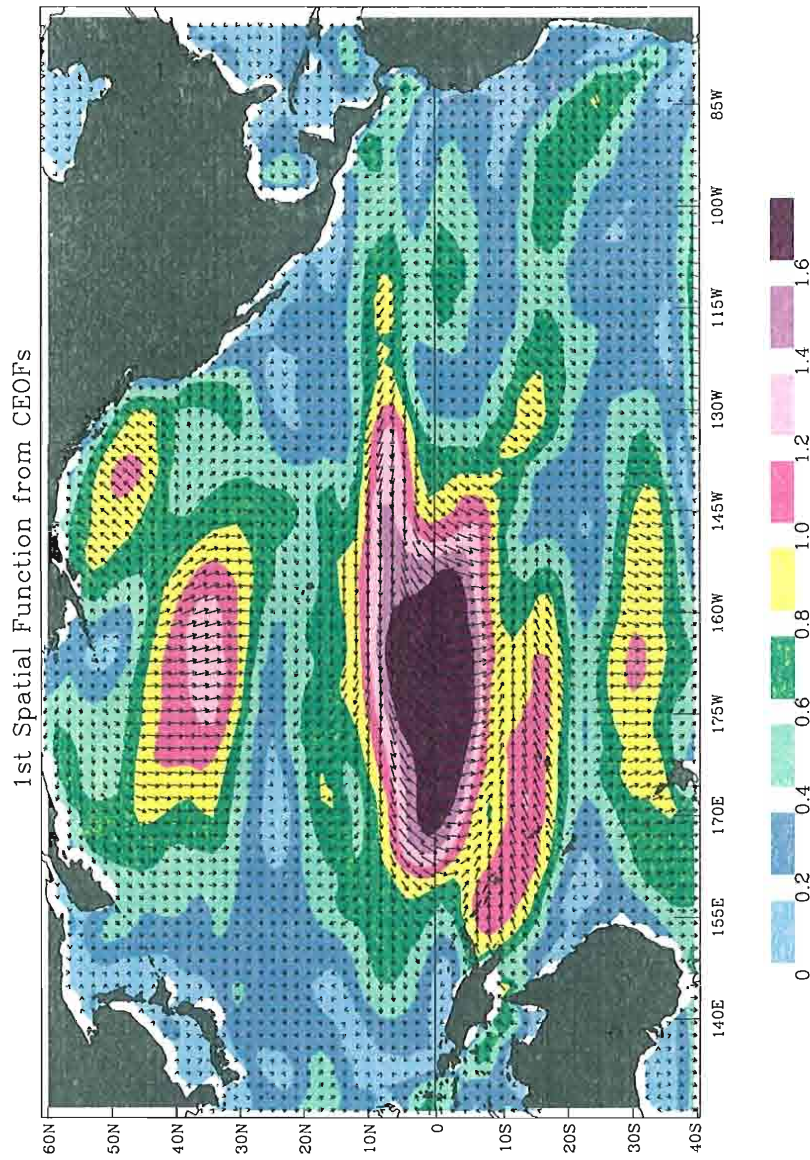


Figure 21: The first spatial function from the CEOF analysis. This field represents 22.76 percent of the variance.

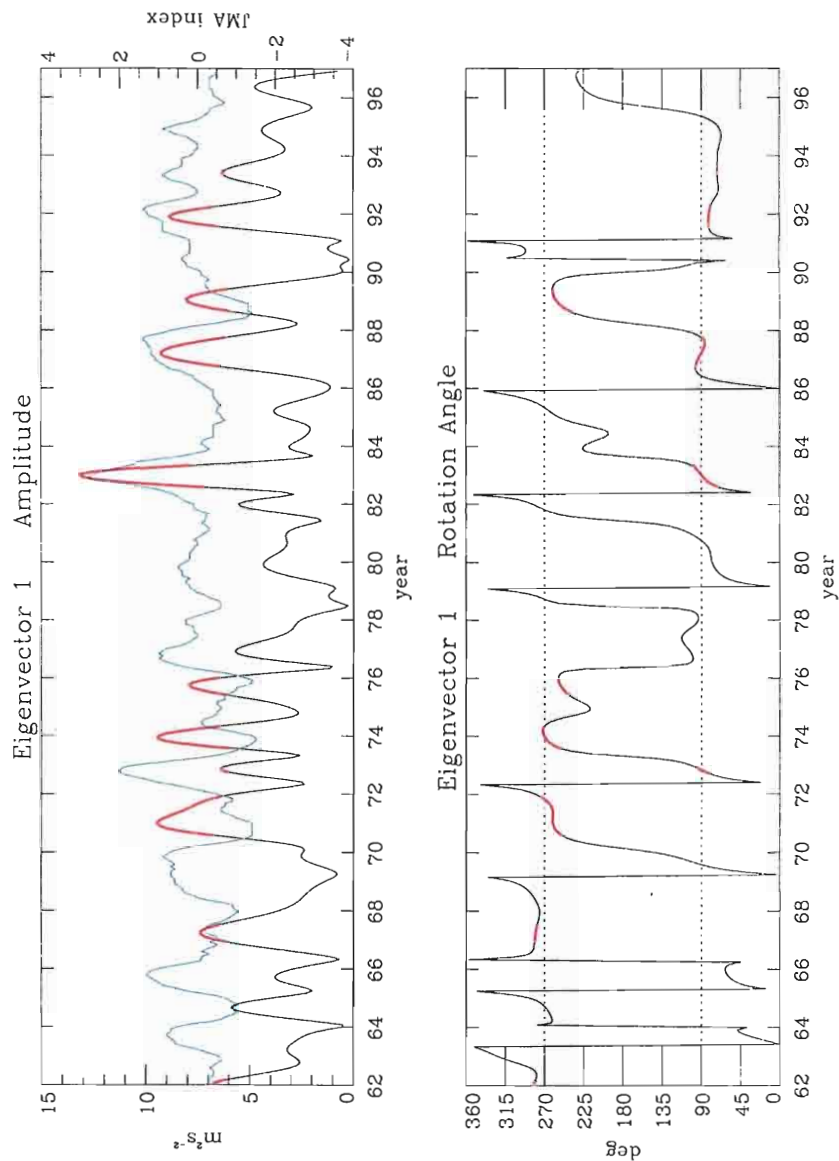


Figure 22: The amplitude(top) and rotation angle(bottom) for the first eigenvector, and JMA SST index(blue). Amplitudes greater than $6m^2s^{-2}$, approximately the largest 20 percent of the amplitudes, are highlighted in red. The rotation angle is in the counterclockwise direction.

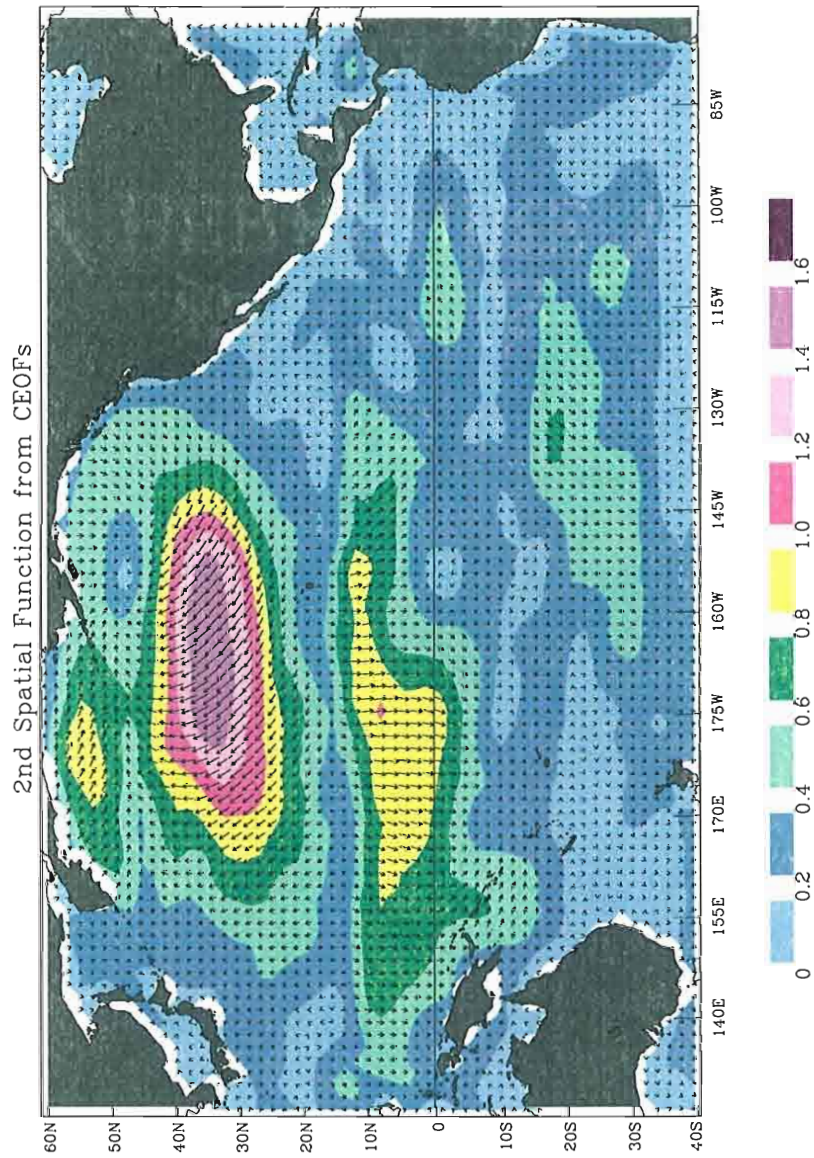


Figure 23: The second spatial function from the CEOF analysis. This field represents 11.16 percent of the variance.

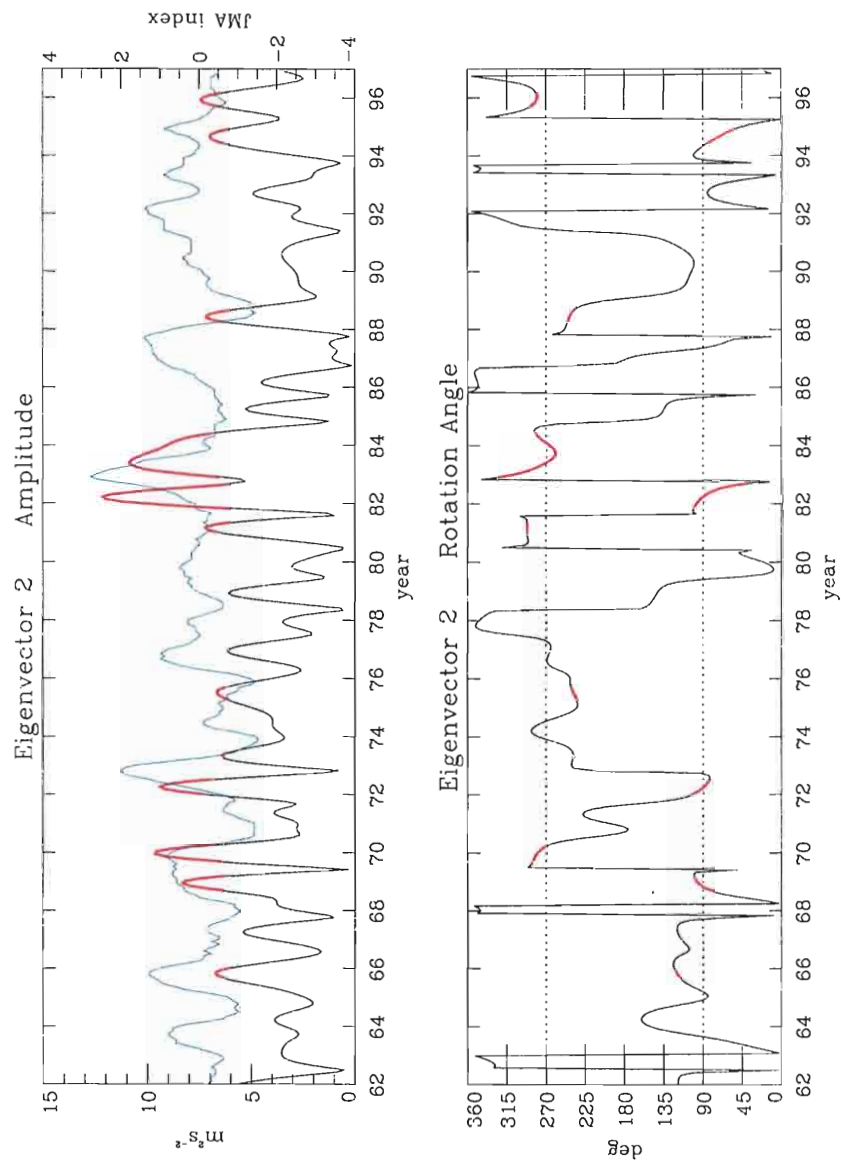


Figure 24: The amplitude(top) and rotation angle(bottom) for the second eigenvector, and JMA SST index(blue). Amplitudes greater than $6m^2s^{-2}$, approximately the largest 20 percent of the amplitudes, are highlighted in red. The rotation angle is in the counterclockwise direction.

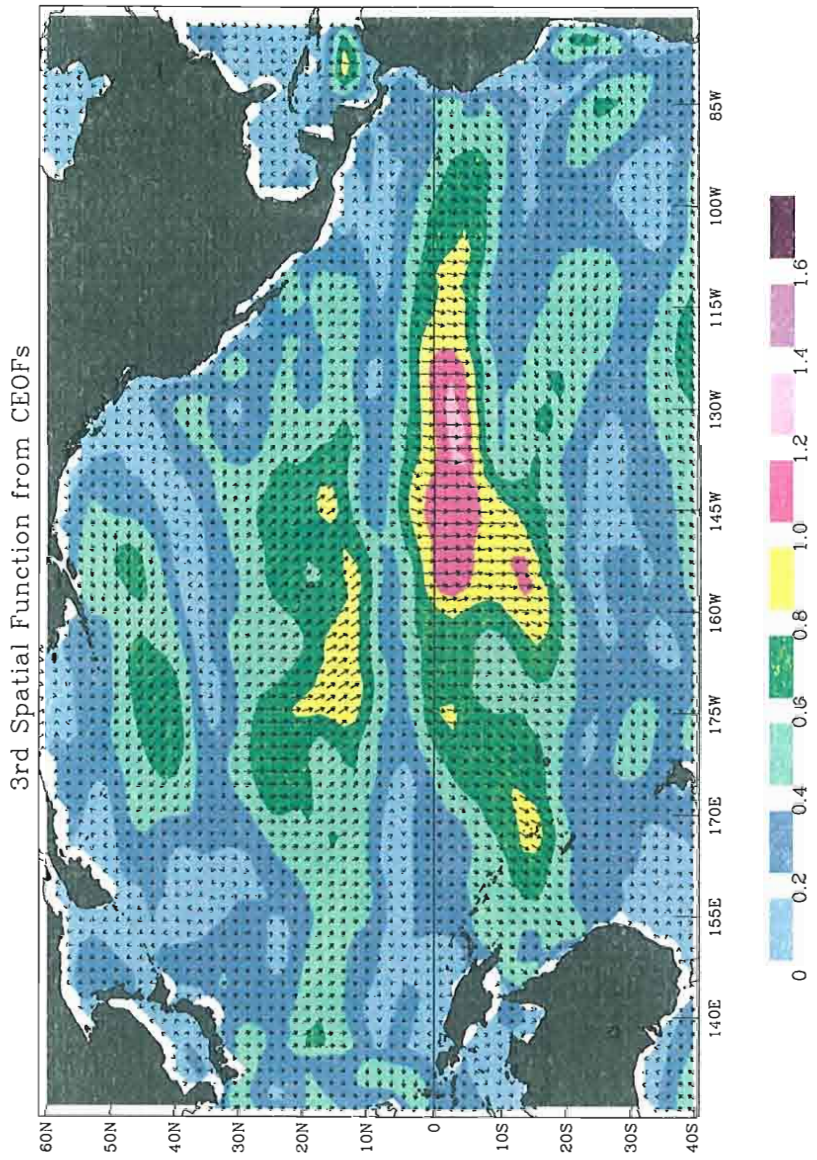


Figure 25: The third spatial function from the CEOF analysis. This field represents 10.01 percent of the variance.

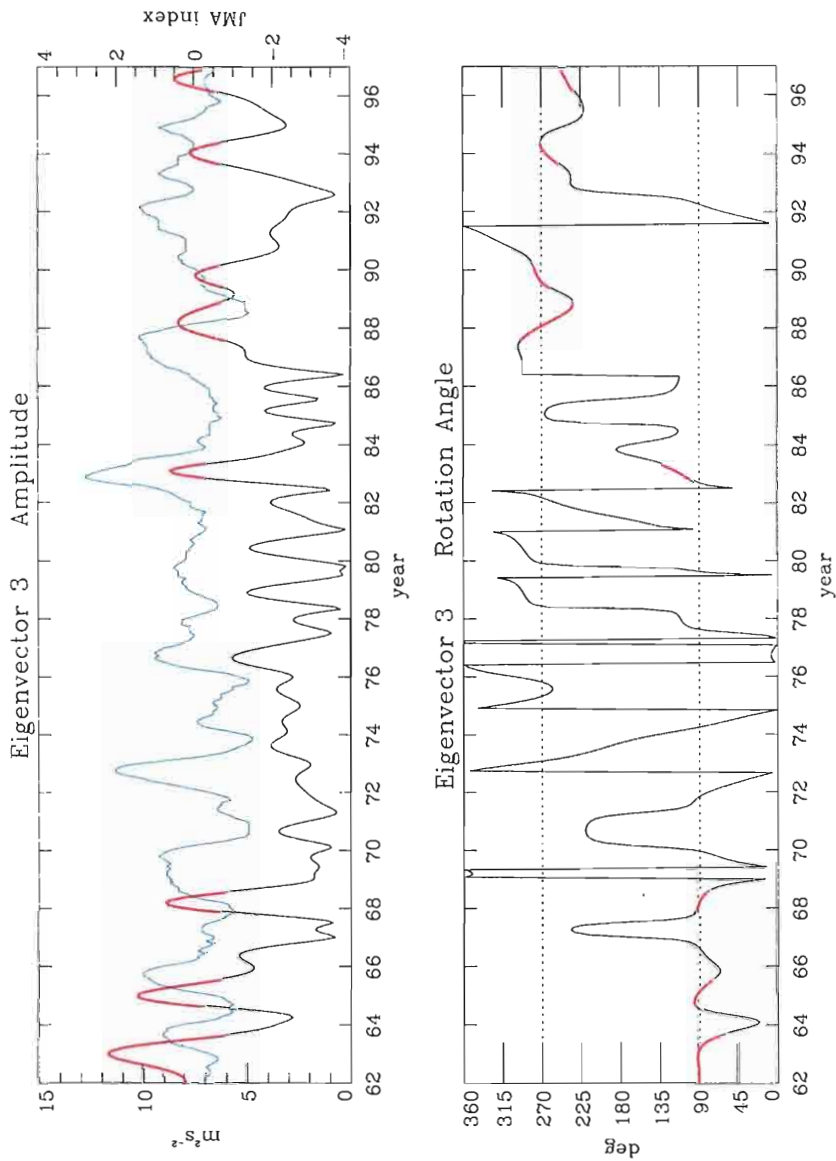


Figure 26: The amplitude(top) and rotation angle(bottom) for the third eigenvector, and JMA SST index(blue). Amplitudes greater than $6m^2s^{-2}$, approximately the largest 20 percent of the amplitudes, are highlighted in red. The rotation angle is in the counterclockwise direction.

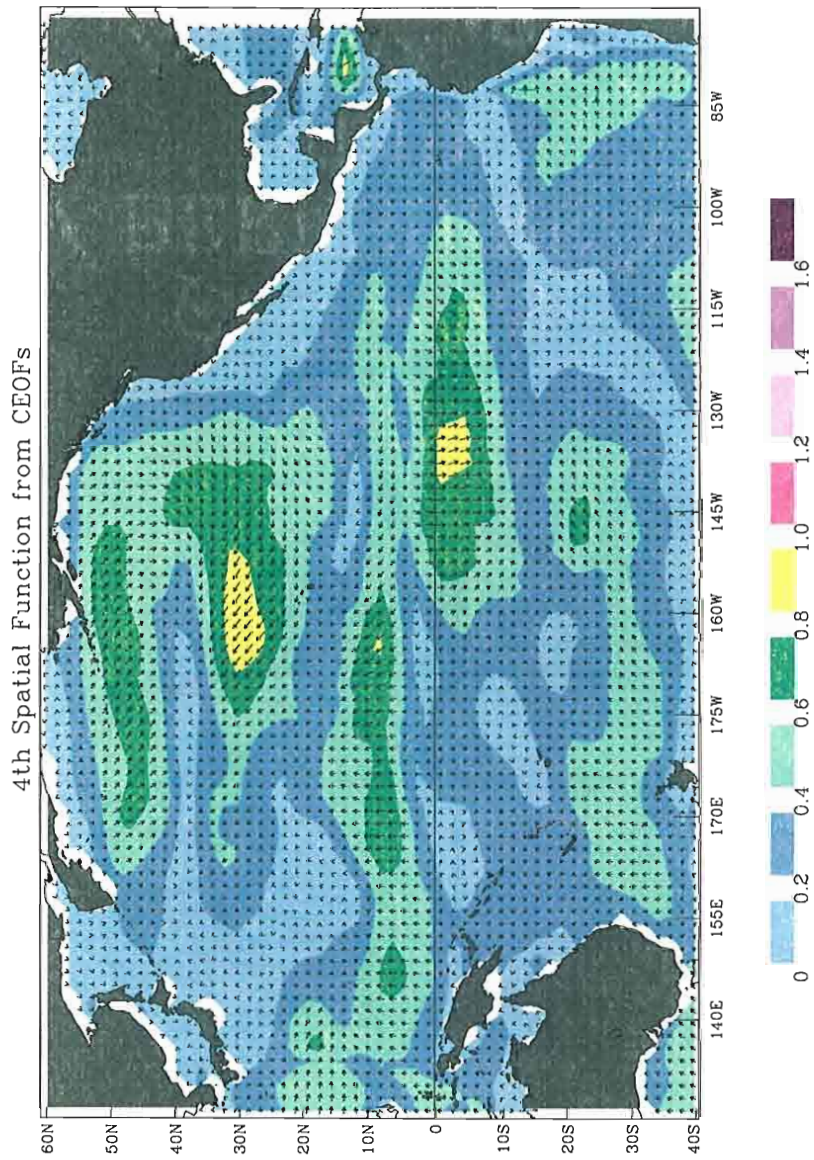


Figure 27: The fourth spatial function from the CEOF analysis. This field represents 7.02 percent of the variance.

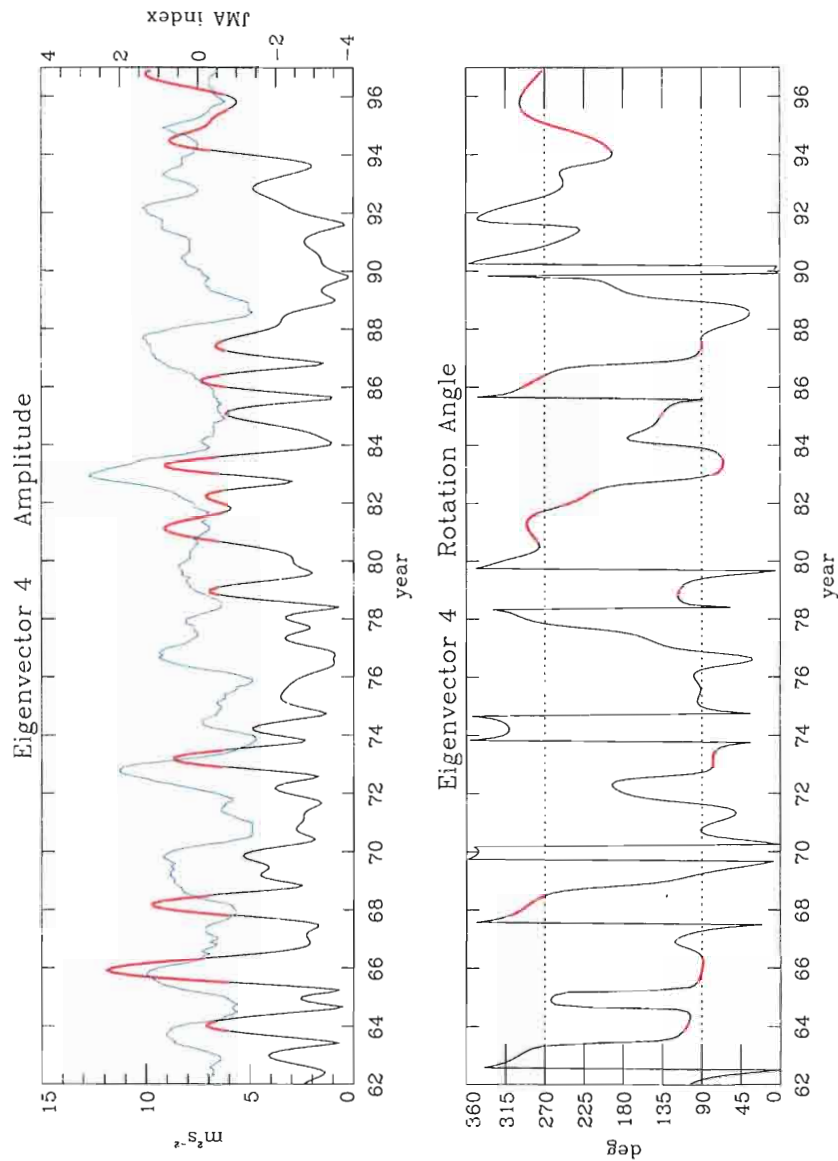


Figure 28: The amplitude(top) and rotation angle(bottom) for the fourth eigenvector, and JMA SST index(blue). Amplitudes greater than $6m^2s^{-2}$, approximately the largest 20 percent of the amplitudes, are highlighted in red. The rotation angle is in the counterclockwise direction.

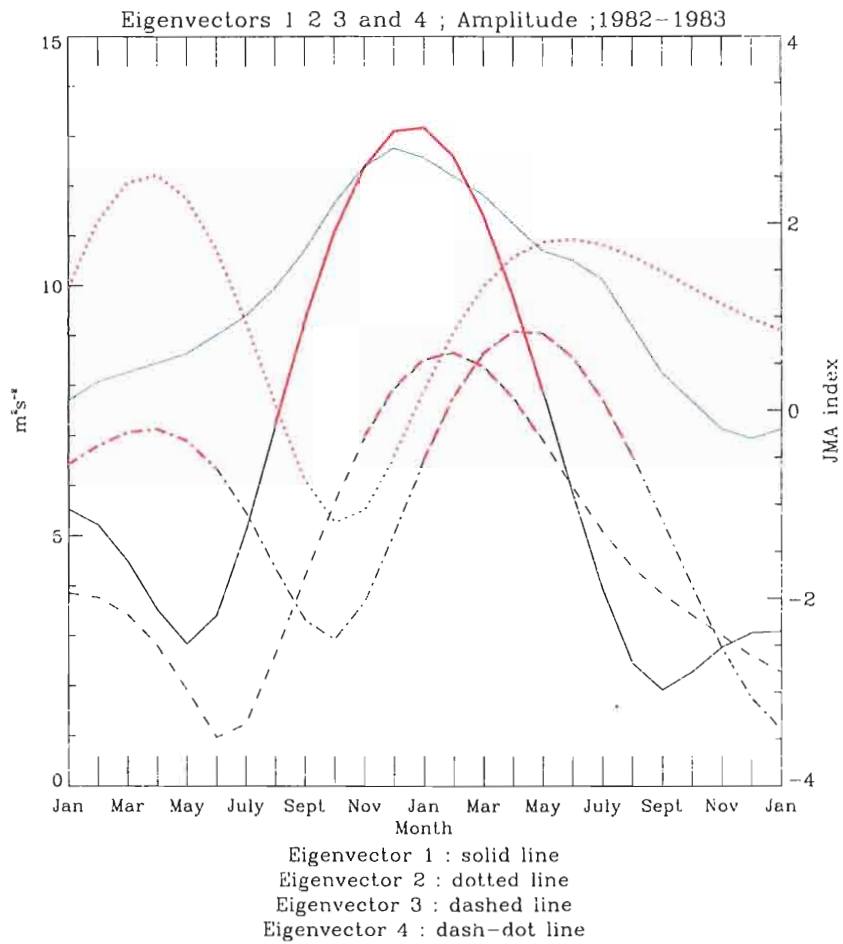


Figure 29: The amplitude for the first through fourth eigenvectors from January of 1982 through December of 1983, and JMA SST anomaly index(blue). Amplitudes greater than $6m^2s^{-2}$, approximately the largest 20 percent of the amplitudes, are highlighted in red.

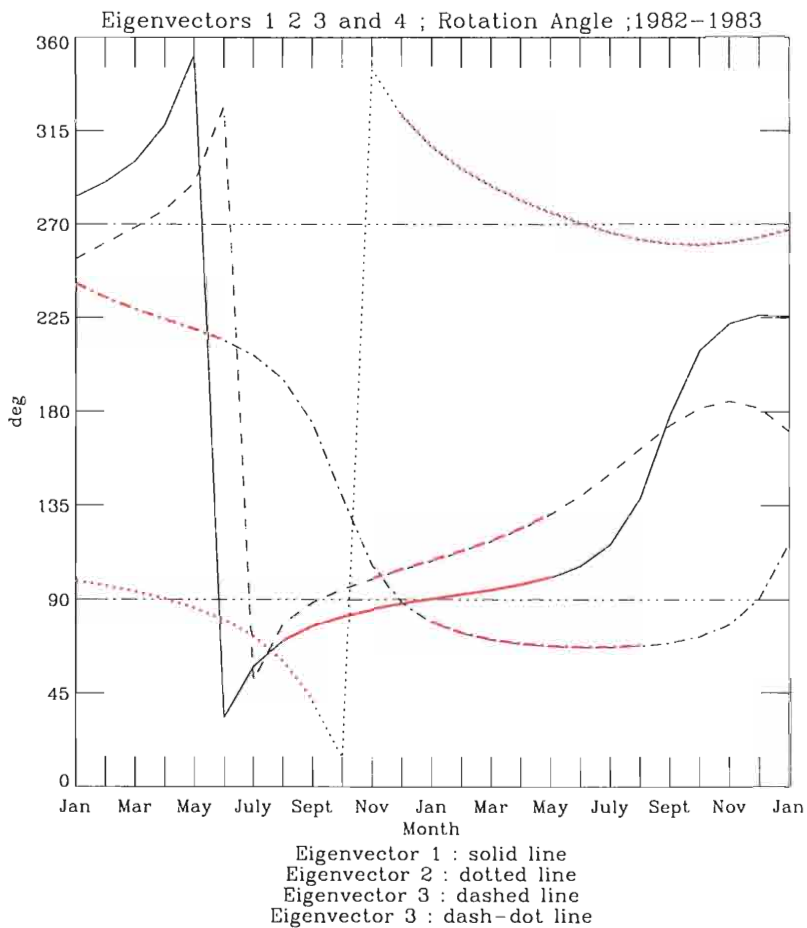


Figure 30: The rotation angle for the first through fourth eigenvectors from January of 1982 through December of 1983. Amplitudes greater than $6m^2s^{-2}$, approximately the largest 20 percent of the amplitudes, are highlighted in red. The rotation angle is in the counterclockwise direction.

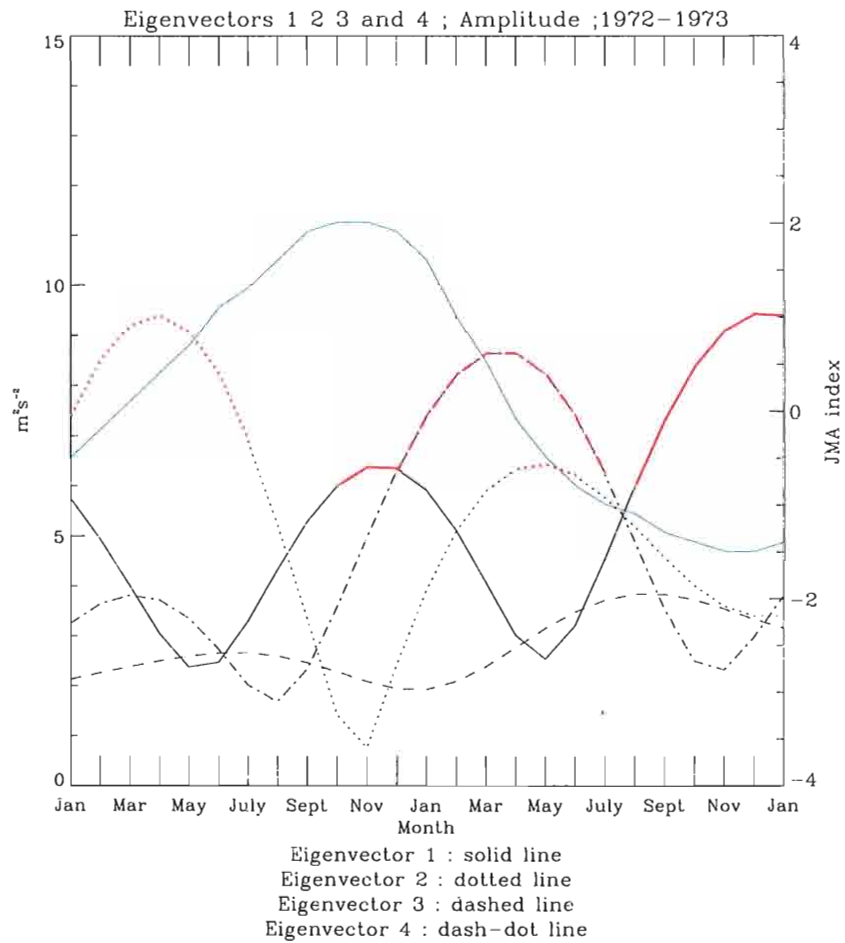


Figure 31: The amplitude for the first through fourth eigenvectors from January of 1972 through December of 1973, and JMA SST anomaly index(blue). Amplitudes greater than $6m^2s^{-2}$, approximately the largest 20 percent of the amplitudes, are highlighted in red.

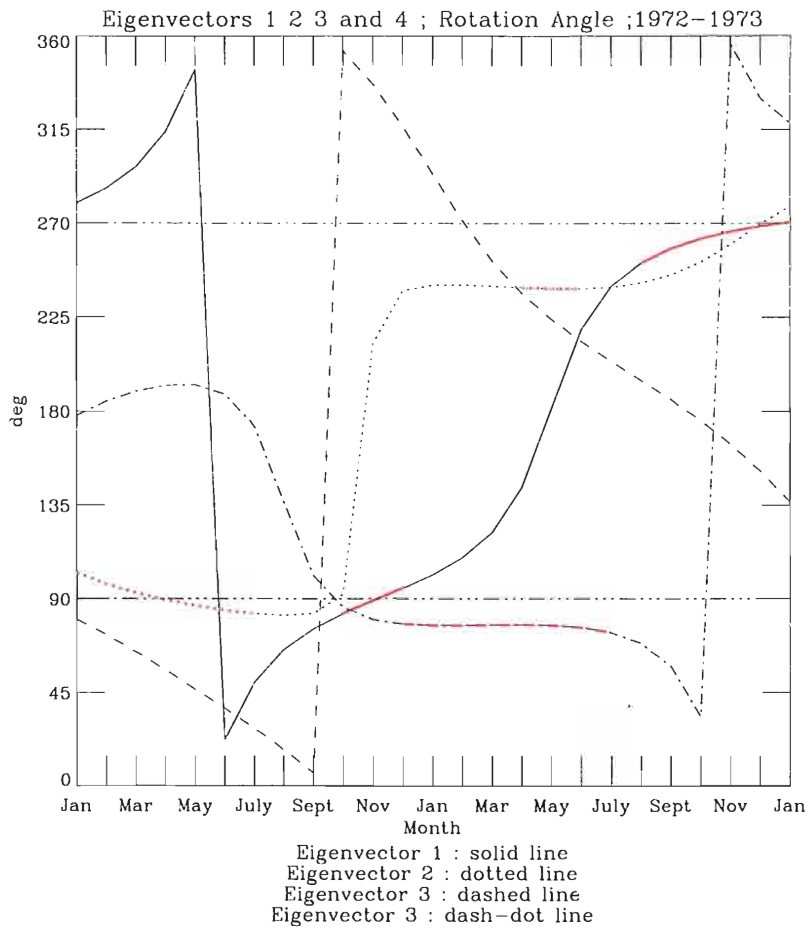


Figure 32: The rotation angle for the first through fourth eigenvectors from January of 1972 through December of 1973. Amplitudes greater than $6m^2s^{-2}$, approximately the largest 20 percent of the amplitudes, are highlighted in red. The rotation angle is in the counterclockwise direction.

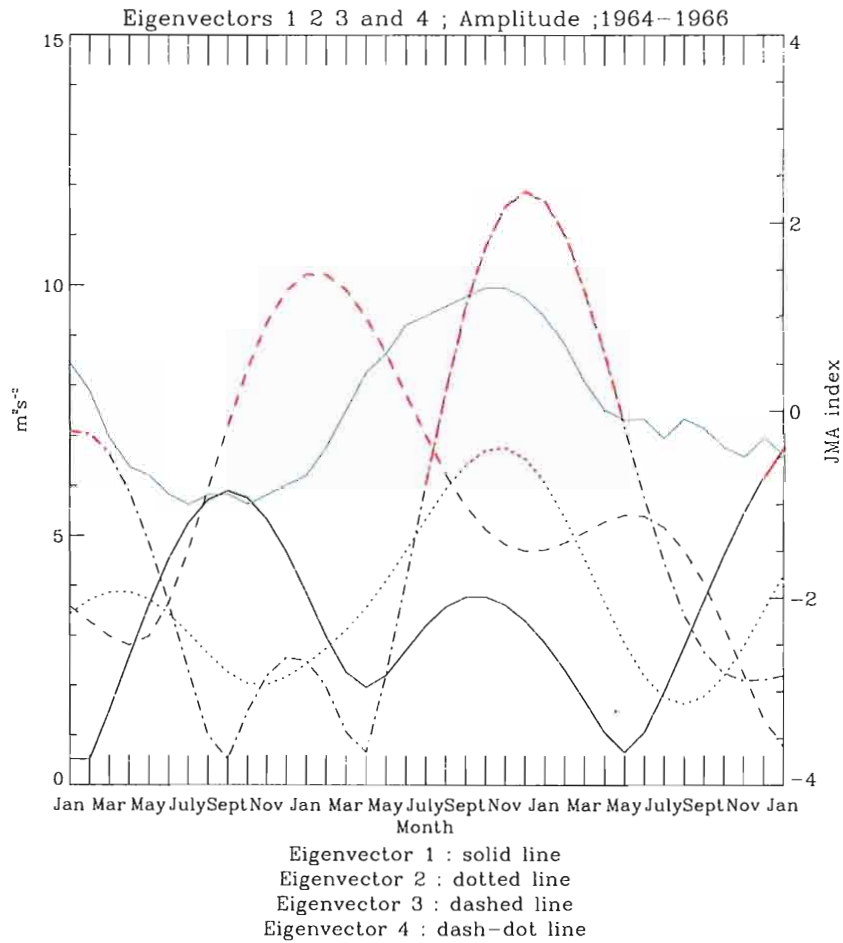


Figure 33: The amplitude for the first through fourth eigenvectors from January of 1964 through December of 1966, and JMA SST anomaly index(blue). Amplitudes greater than $6m^2s^{-2}$, approximately the largest 20 percent of the amplitudes, are highlighted in red.

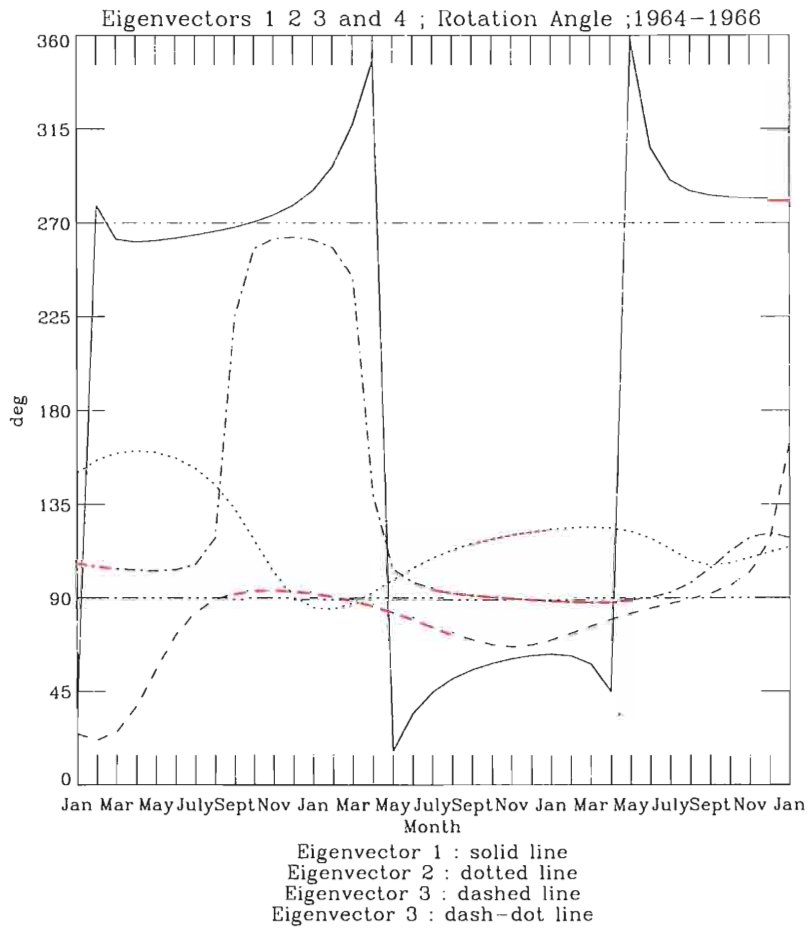


Figure 34: The rotation angle for the first through fourth eigenvectors from January of 1964 through December of 1966. Amplitudes greater than $6m^2s^{-2}$, approximately the largest 20 percent of the amplitudes, are highlighted in red. The rotation angle is in the counterclockwise direction.

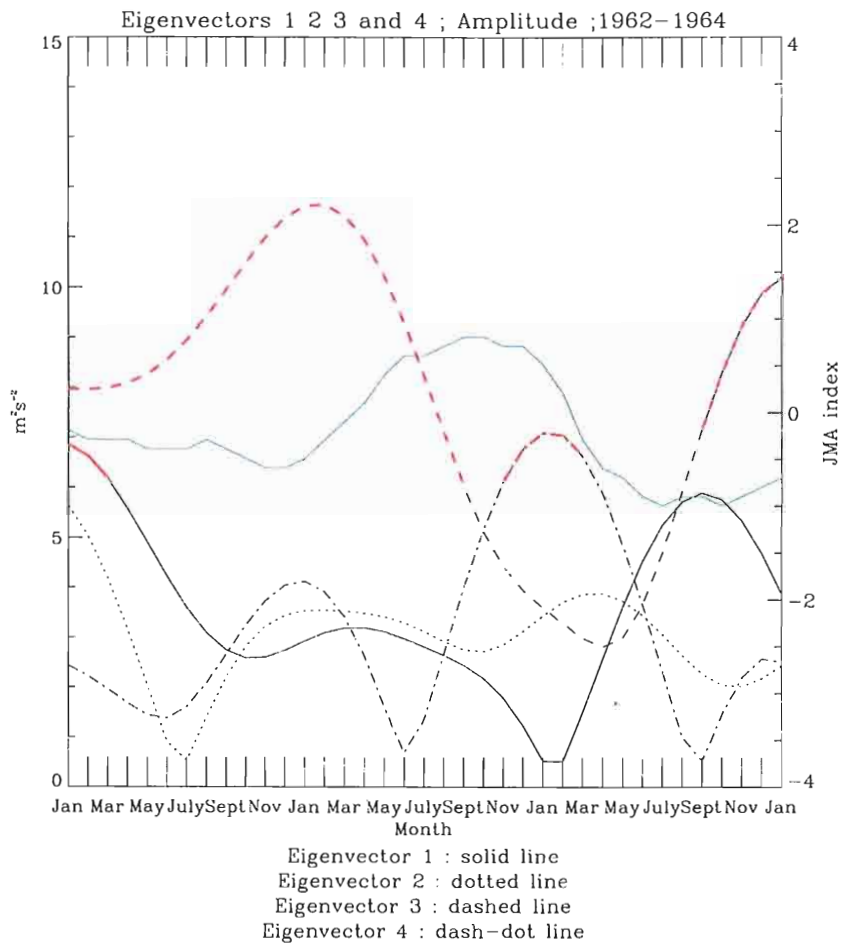


Figure 35: The amplitude for the first through fourth eigenvectors from January of 1962 through December of 1963, and JMA SST anomaly index(blue). Amplitudes greater than $6m^2s^{-2}$, approximately the largest 20 percent of the amplitudes, are highlighted in red.

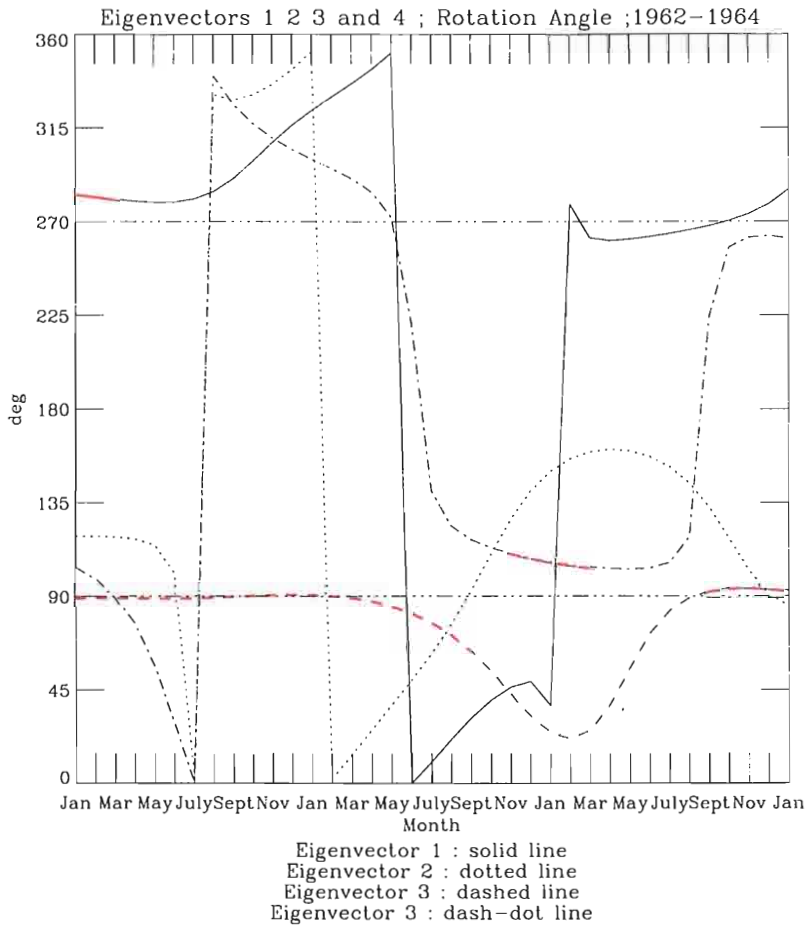


Figure 36: The rotation angle for the first through fourth eigenvectors from January of 1962 through December of 1963. Amplitudes greater than $6m^2s^{-2}$, approximately the largest 20 percent of the amplitudes, are highlighted in red. The rotation angle is in the counterclockwise direction.

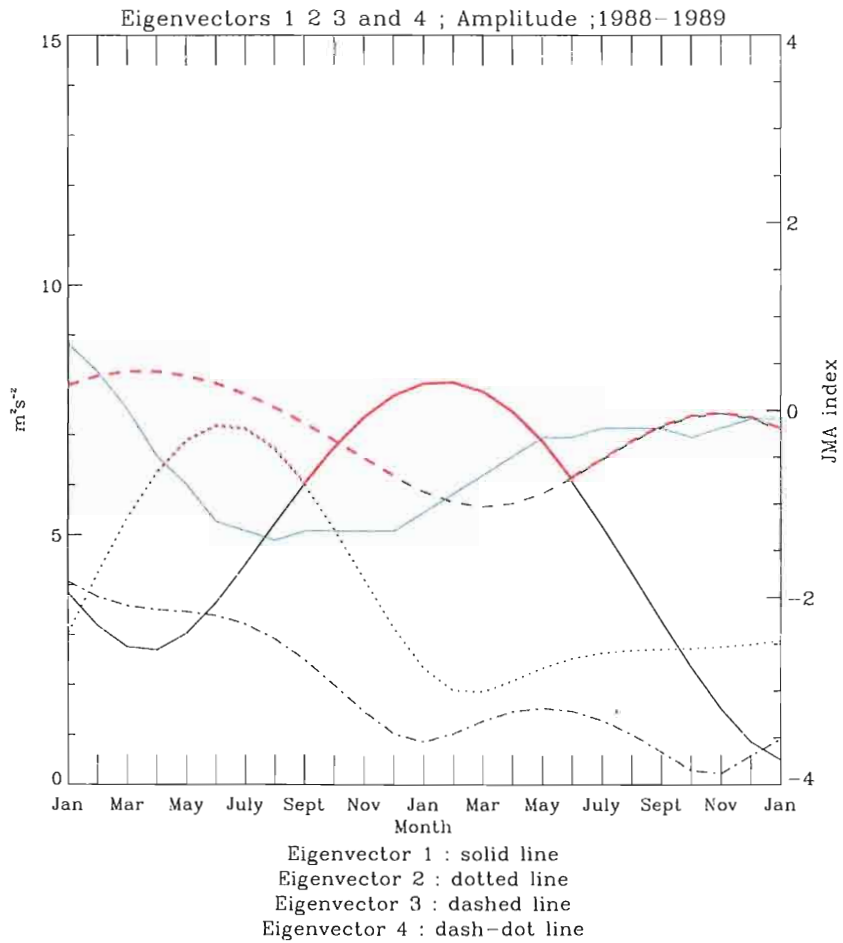


Figure 37: The amplitude for the first through fourth eigenvectors from January of 1988 through December of 1989, and JMA SST anomaly index(blue). Amplitudes greater than $6m^2s^{-2}$, approximately the largest 20 percent of the amplitudes, are highlighted in red.

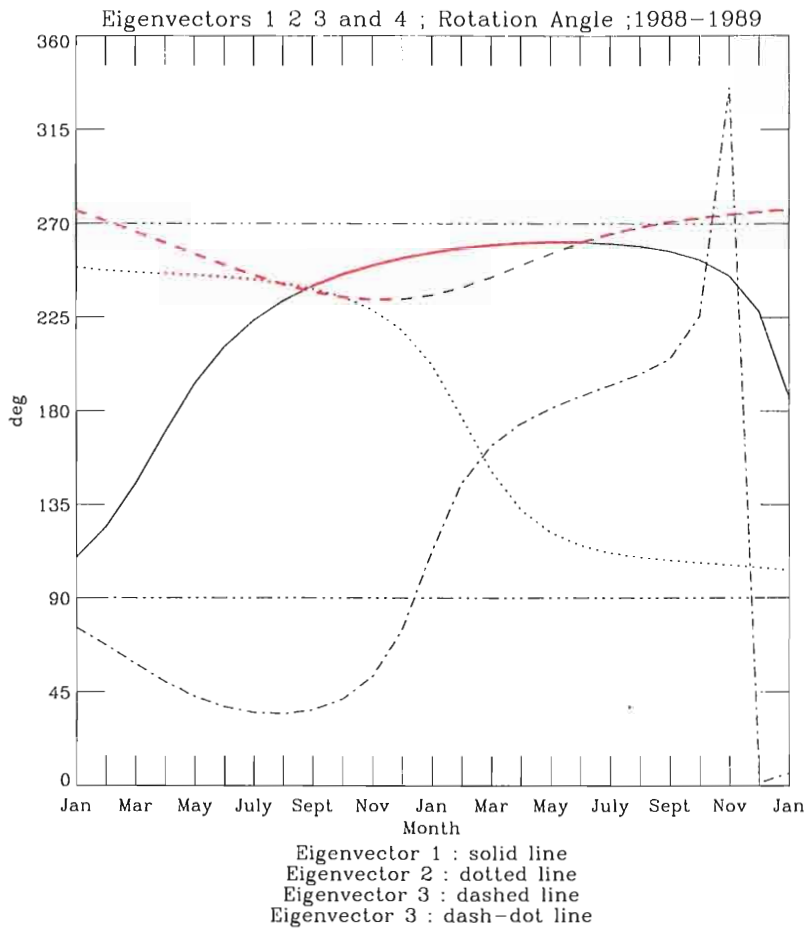


Figure 38: The rotation angle for the first through fourth eigenvectors from January of 1988 through December of 1989. Amplitudes greater than $6m^2s^{-2}$, approximately the largest 20 percent of the amplitudes, are highlighted in red. The rotation angle is in the counterclockwise direction.

5. SUMMARY

A variational blending method is applied in the assimilation of FSU and NCEP reanalysis 10-meter pseudostress over the Pacific Ocean. This is accomplished through the minimization of a strategically designed cost function, consisting of weighted misfit constraints for the FSU and NCEP reanalysis fields, as well as Laplacian and kinematic terms included to insure smoothness in the derivative fields of the solution. Subjective selection of spatially dependent weighting functions for the FSU and NCEP constraints allows us to produce the optimal combination of the two fields based on each datasets regional strengths. A sensitivity analysis is performed to determine the weights for the Laplacian and kinematic constraints. The sensitivity analysis reveals that the Laplacian produces the largest response in the solution fields, where as the solution is more sensitive to small changes in the divergence and curl weights.

The variational blending approach produces the desired results in the solution fields. The minimization solution in the tropical Pacific, the FSU region of influence, is a smoothed version of the FSU pseudostress fields. The solution fields gradually change through the transition zone into the NCEP reanalysis region of influence. The derivative fields of the minimization solution maintain the physical properties of the FSU and NCEP analyses without producing any artificial noise along the border of the two fields. This result is in part due to the gradual transition zones in the weighting functions, but primarily due to the smoothing effects of the Laplacian and kinematic constraints.

The completeness of the blended pseudostress fields allows us to examine the kinematic constraints.

The completeness of the blended pseudostress fields allows us to examine the variability of tropical and extratropical pseudostress over the Pacific Ocean through

a CEOF analysis. The NCEP reanalysis 10-meter pseudostress, from 40° N to 60° N, is added to the northern edge of the domain, and the monthly climatological means, as calculated from the blended product, are removed. The pseudostress anomalies are filtered in time with an 18-month low-pass Kaylor filter (*Kaylor (1977)*). The CEOF analysis highlights interannual pseudostress variability over the Pacific from 1962-1997.

The first mode represents the typical mature phase of the El Niño and El Viejo events. This mode exhibits the classic El Niño pseudostress anomaly pattern over the tropical Pacific, and a strengthening of the Aleutian low during the mature phases of the El Niños of 1973, 1983, 1987, and 1992. The pattern is reversed for the El Viejo events during the time period, which are preceded by the combined effects of the second and third modes. Therefore, the CEOF analysis links the strengthening of the Aleutian low to the classic El Niño pseudostress anomaly pattern. This link has been shown to exist in observed geopotential height, as well as model height fields, over the North Pacific during El Niño winters in the northern hemisphere (*Horel and Wallace (1981)* and *Lau (1997)*).

The second and fourth modes represent the precursor modes during the winter-spring prior to the 1973, and 1983 El Niños. This precursor appears in the form of northwesterly anomalies developing in the western equatorial Pacific and weakened northeast trades, coincident with a weakening of the Aleutian low. Surface pressure analyses have shown that the Aleutian low is weakened in the winter preceding an El Niño event (*Emery and Hamilton (1985)*); the second mode provides further evidence of this in our pseudostress analyses. The second and fourth modes also appear during the end of these two El Niño events, marking the return to normal of the equatorial anomalies in the western Pacific. At the same time, these modes contribute to the strengthened Aleutian low which is shifted southeast of its normal position.

The third mode appears during the 1983 event representing northwesterly anomalies in the western equatorial Pacific and strengthened northeast trades, coincident with a strengthening of the Aleutian low which is shifted southeast of its normal position.

The third mode appears during the 1983 event representing northwesterly anoma-

lies in the eastern equatorial Pacific, after the peak of the first mode. This mode also appears during the onset of the El Niños of the 1960's. The combined contributions of the second through fourth modes explain the sequence of events for the 1963, 1965, and 1969 El Niños; the first mode is not significant during these weak events. The El Niño events of the 1960's have been shown to be a result of the cessation of the normal semiannual variability of the easterlies in the central Pacific (*Busalacchi and O'Brien* (1981)). Thus, these events are not represented by the first mode which represents an anomalous relaxation of the easterlies in the central equatorial Pacific.

Each ENSO event has its own individual characteristics. Some generalizations regarding development and extratropical connections are possible, however no two events are completely identical. The CEOF analysis in this study reveals many similarities between events (e.g., 1973 and 1983 events), as well as significant variability between events (e.g., the El Niños of the 1960's).

REFERENCES

- Beale, E. M., *A derivation of conjugate-gradients. Numerical methods for non-linear optimization*, F. A. Lootsma, Ed., Academic Press, 1972.
- Busalacchi, A. J., and J. J. O'Brien, Interannual variability of the equatorial Pacific in the 1960's, *J. of Geophys. Res.*, *86*, 10901-10907, 1981.
- da Silva, A. M., C. C. Young, and S. Levitus, Atlas of surface marine data 1994 volume 1: Algorithms and procedures, technical report, NOAA, Atlas NESDIS 6, 1994.
- Emery, W. J., and K. Hamilton, Atmospheric forcing of interannual variability in the Northeast Pacific Ocean: Connections with El Niño, *J. of Geophys. Res.*, *90*, 857-868, 1985.
- Fischer, M., M. Latif, M. Flugel, and M. Ji, The impact of data assimilation on ENSO simulations and predictions, *Mon. Wea. Rev.*, *125*, 819-829, 1997.
- Hoffman, R. N., SASS wind ambiguity removal by direct minimization. part II: Use of smoothness and dynamical constraint, *Mon. Wea. Rev.*, *112*, 1829-1852, 1984.
- Horel, J. D., Complex principle component analysis: theory and examples, *J. of Clim. and Applied Met.*, *23*, 1660-1673, 1984.
- Horel, J. D., and J. M. Wallace, Planetary-scale atmospheric phenomena associated with the southern oscillation, *Mon. Wea. Rev.*, *109*, (4), 813-829, 1981.
- Kalnay, E., M. Kanamitsu, R. Kistler, W. Collins, D. Deaven, L. Gandin, M. Iredell, S. Saha, G. White, J. Woollen, Y. Zhu, M. Chelliah, W. Ebisuzaki, W. Higgins, J. Janowiak, K. C. Mo, C. Ropelewski, J. Wang, A. Leetma, R. Reynolds, R. Jenne, and D. Joseph, The NCEP/NCAR 40-year reanalysis project, *Bull. of the Amer. Met. Soc.*, *77*, (3), 437-471, 1996.
- Kaylor, R. E., Filtering and decimation of digital time series, technical report, Institute for Physical Science and Technology, BN 850, 1977.
- Landsteiner, M. C., M. J. McPhaden, and J. Picaut, On the sensitivity of Sverdrup transport estimates to the specification of wind stress forcing in the tropical Pacific, *J. Geophys. Res.*, *95*, 1681-1692, 1990.
- Lau, N.-C., Interactions between global SST anomalies and the midlatitude atmospheric circulation, *Bull. of the Amer. Met. Soc.*, *78*, (1), 21-33, 1997.
- Lau, N.-C., Interactions between global SST anomalies and the midlatitude atmospheric circulation, *Bull. of the Amer. Met. Soc.*, *78*, (1), 21-33, 1997.

- Legler, D. M., Empirical orthogonal function analysis of wind vectors over the tropical Pacific region, *Bull. of the Amer. Met. Soc.*, *64*, (3), 234–241, 1983.
- Legler, D. M., I. M. Navon, and J. J. O'Brien, Objective analysis of pseudostress over the Indian Ocean using direct minimization approach, *Mon. Wea. Rev.*, *117*, 709–720, 1989.
- Lorenc, A. C., Analysis methods for numerical weather prediction, *Quat. J. Roy. Meteor. Soc.*, *112*, 1177–1194, 1986.
- McPhaden, M. J., A. J. Busalacchi, and J. Picaut, Observations and wind-forced model simulations of the mean seasonal cycle in the tropical Pacific sea surface topography, *J. Geophys. Res.*, *93*, 8131–8146, 1988.
- Meyers, S. D., C. S. Jones, D. M. Legler, and J. J. O'Brien, The sensitivity of parametric variations in direct minimization techniques, *Mon. Wea. Rev.*, *122*, (7), 1632–1639, 1994.
- Navon, I. M., and D. M. Legler, Conjugate-gradient methods for large-scale minimization in meteorology, *Mon. Wea. Rev.*, *115*, 1479–1502, 1987.
- North, R. G., T. L. Bell, R. F. Cahalan, and F. J. Hoeng, Sampling errors in the estimation of empirical orthogonal functions, *Mon. Wea. Rev.*, *110*, 699–706, 1982.
- Rasmusson, E. M., and T. H. Carpenter, Variations in tropical sea surface temperature and surface wind fields associated with the southern oscillation/El Niño, *Mon. Wea. Rev.*, *110*, (5), 354–384, 1982.
- Shanno, D. F., and K. H. Phua, Remark on algorithm 500-a variable method subroutine for unconstrained nonlinear minimization, *ACM Trans. on Mathematical Software*, *6*, 618–622, 1980.
- Stricherz, J. N., D. M. Legler, and J. J. O'Brien, TOGA pseudo-stress atlas 1985-1994: II tropical Pacific Ocean, technical report, COAPS/Florida State University, COAPS Report 97-2, 1997.
- Tourre, Y. M., and W. B. White, ENSO signals in global upper-ocean temperature, *J. of Phys. Ocn.*, *25*, (6), 1317–1332, 1995.
- Wilks, D. S., *Statistical Methods in Atmospheric Sciences*, Academic Press Inc., 1995.
- Zebiak, S. E., Diagnostic studies of Pacific surface winds, *J. of Clim.*, *3*, 1016–1031, 1990.

BIOGRAPHICAL SKETCH

Degrees

M.S. anticipated July 1998, Meteorology, Florida State University, Tallahassee, Florida.

Thesis title: "Assimilation of FSU and NCEP Reanalysis Pseudostress Products Over the Pacific Ocean and Complex EOF Analysis of the Resulting Fields."

B.S. May 1996, Physical Science, University of Maryland at College Park, Maryland.

Experience

Florida State University. Center for Ocean-Atmospheric Prediction Studies(COAPS). Graduate student research. Project involved the application of spatially dependent data assimilation to synthesize Florida State University(FSU) and NCEP Reanalysis wind data over the Pacific Ocean. Vector empirical orthogonal function(EOF) analysis of the resulting fields highlighted the relationship between extratropical and tropical regions on interannual time periods.

University of Maryland at College Park, Meteorology Department. Undergraduate student research. Project involved the study of high ozone events in the Washington D.C. area through the creation and interpretation of back student research. Project involved the study of high ozone events in the Washington D.C. area through the creation and interpretation of back trajectory plots. 1995-1996.

University of Maryland at College Park, College of Computer, Mathematical, and Physical Sciences Dean's Office. Student assistant. 1994-1996.

University of Hawaii - Manoa. National Student Exchange(NSE) participant. Studied environmental and physical science at the University of Hawaii through the NSE program. 1993.

University of Hawaii - Manoa. NSE. Treasurer, NSE Student Association. 1993.

Course work

Atmospheric data assimilation. Air-sea interactions. Dynamical weather prediction. Time series analysis. Tropical meteorology. Satellite and remote sensing of planetary atmospheres. Cloud physics. Synoptic, dynamical, and physical meteorology. Physical oceanography. Partial differential equations, physics, and chemistry.

Computer experience

Experience with Unix, Windows(95 and NT), PC, and Mac operating systems as well as SGI and SUN workstations.

Experience with various word processing and spreadsheet software (MS Works, Word, Word Perfect, Quatro Pro, Excel). Use of GEMPAK and MCIDAS weather graphic software. Experience with \LaTeX for technical writing.

Programming experience in IDL and Fortran. Utilized IDL in the development of contour and vector plotting subroutines for large and small data sets.

Developed 2-dimensional and 3-dimensional animation subroutines in IDL.

Applied moving vector routines in IDL for vector animations. Use of GrADS in back trajectory plotting. HTML programming experience in web page development.

Applied moving vector routines in IDL for vector animations. Use of GrADS in back trajectory plotting. HTML programming experience in web page development.

Honors

Golden Key National Honor Society.

Chi Epsilon Pi, National Meteorology Honor Society.

Personal information

Born 19 October 1973, Bremerton, Washington

Please feel free to contact my current supervisor, Dr. James O'Brien, at
(850)644-4581.